THE ASTROPHYSICAL JOURNAL, 466:317–337, 1996 July 20

THE NOBEYAMA MILLIMETER ARRAY SURVEY OF YOUNG STELLAR OBJECTS ASSOCIATED WITH THE TAURUS MOLECULAR CLOUD

NAGAYOSHI OHASHI
Harvard-Smithsonian Center for Astrophysics, 60 Garden Street, Cambridge, MA 02138; and Nobeyama Radio Observatory, Nobeyama, Minamisaku, Minamimaki, Nagano 384-13, Japan; nohashi@cfa.harvard.edu

MASAHIKO HAYASHI
SUBARU Project Office, National Astronomical Observatory, Mitaka, Tokyo 181, Japan; masa@optik.mtk.nao.ac.jp

AND

RYOHEI KAWABE AND MASATO ISHIGURO
Nobeyama Radio Observatory, Nobeyama, Minamimaki, Minamisaku, Nagano 384-13, Japan; kawabe@nro.nao.ac.jp, ishiguro@nro.nao.ac.jp

Received 1995 October 23; accepted 1996 February 1

ABSTRACT

We have carried out an interferometric survey of 3 mm continuum and CS ($J = 2$–1) line emissions from 13 optically invisible protostar candidates and six young T Tauri stars associated with the Taurus molecular cloud. The survey was made using the Nobeyama Millimeter Array with a spatial resolution of 2″.8–10″. The continuum emission was detected from two protostar candidates and five T Tauri stars and was well coincident with optical or infrared objects. It was not spatially resolved and most probably originated from compact circumstellar disks. The CS emission was detected around 11 protostar candidates and two T Tauri stars. The detected CS condensations are extended, with a typical size and mass of $\sim$2000 AU and 0.01 $M_\odot$, respectively.

Among the eleven protostar candidates with detectable CS emission, seven sources, i.e., IRAS 04016+2610 (L1489), IRAS 04169+2702, IRAS 04191+1503, IRAS 04239+2436, L1551–IRS 5, IRAS 04325+2402, and IRAS 04365+2535, have the CS emission well coincident with infrared sources, while the other four show the CS emission separated away from known infrared sources. Most of the CS emission for the former sources may arise from the innermost part of their protostellar envelopes, while that for the latter sources may originate from compact, dense gas in the vicinity of the infrared sources. The CS gases toward L1489 and IRAS 04365+2535 have disklike structures of $\sim$1500 and $\sim$500 AU in radius, respectively, with velocity gradients along their major axes. The velocity gradient of the disklike structure around L1489 may be due to rotation, while the origin of velocity gradient around IRAS 04365+2535 is not clear. L1551–IRS 5 shows compact CS emission, possibly arising from a disk, together with weak extended features that may be attributed to a denser part of the outflow. The distribution of CS emission around IRAS 04368+2557 (L1527) is anticorrelated with its molecular outflow, suggesting that the CS gas may be a dense shell swept up by the outflow.

The 3 mm continuum detectability toward the protostar candidates is significantly smaller than what we would expect from the statistics of T Tauri disks, which we consider may be due to an evolutionary effect; namely, during the transitional phase from embedded protostars to revealed T Tauri stars, either the disk mass has rapidly increased, or dust particles in the disks have grown significantly, or both. For the embedded protostar candidates, the CS intensity is correlated with bolometric luminosity. This may mean that the final stellar mass is correlated with the mass of dense cores.

Subject headings: circumstellar matter — ISM: individual (Taurus molecular cloud) — ISM: molecules — radio lines: ISM — stars: pre–main-sequence

1. INTRODUCTION

This paper describes results of high–angular resolution observations carried out with the Nobeyama Millimeter Array (NMA) of young stellar objects associated with the Taurus molecular cloud. In a previous paper (Ohashi et al. 1991, hereafter Paper I), we presented observations of the CS ($J = 2$–1) and 3 mm continuum emissions from six embedded protostellar objects and five young T Tauri stars. Since that contribution, we have completed a survey of 13 embedded sources and six young T Tauri stars selected from the *IRAS* catalog.

Recent observations have revealed that many T Tauri stars are associated with compact and dense circumstellar dust disks (Strom et al. 1989; Beckwith et al. 1990; Adams, Emerson, & Fuller 1990). Dust emissions at millimeter and submillimeter wavelengths have shown that the disks have masses and sizes ranging from 10^{-3} to 1 $M_\odot$ and 10 to 100 AU, respectively. These parameters are similar to those of a "protosolar nebula" (e.g., Hayashi, Nakazawa, & Nakagawa 1985); the disks are believed to be "protoplanetary disks."

In addition to their physical properties, evolution of such circumstellar disks is of great importance for understanding the mechanism of planetary system formation and is now a field of active investigation. This evolution may be roughly divided into two phases: the formation phase and the dissipation phase. Observations of T Tauri stars have provided information on the dissipation of circumstellar disks. Strom et al. (1989) and Skrutskie et al. (1990) observed the decrease of near- and midinfrared excess emission with the age of T Tauri stars, suggesting the dissipation of the inner $\lesssim$1 AU region of the disks. This is consistent with the implication

TABLE 1

OBSERVED SOURCES WITH NMA

OBSERVED SOURCE (1)	REFERENCE (2)	FIELD CENTER R.A. (1950) (3)	FIELD CENTER Decl. (1950) (4)	REFERENCE (5)	OPTICAL APPEARANCE (6)	log (F_{12}/F_{25})[a] (7)	F_{100}[b] (Jy) (8)	L_{bol}[c] ($L_\odot$) (9)	REFERENCE (10)
L1489	1, 2	$4^h01^m40^s.4$	26°10′47″.0	10	Invisible	−0.64	56	3.7	16
04108+2803.....	2	4 10 49.3	28 03 58.0	10	Invisible	−0.65	11	0.64	16
04154+2823.....	2	4 15 25.7	28 23 56.0	10	Invisible	−0.35	< −7.8	0.33	2
04169+2702.....		4 16 54.6	27 02 49.0	10	Invisible	−0.84	17	0.74	16
04191+1523.....		4 19 08.5	15 23 16.0	10	Invisible	< −0.71	14	0.48	17
04239+2436.....	2	4 23 55.2	24 36 54.0	10	Invisible[d]	−0.61	16	1.2	16
04248+2612.....	2	4 24 52.7	26 12 42.0	11	Invisible[d]	−0.57	9.3	0.35	16
L1551-IRS 5.....	3, 4	4 28 40.2	18 01 42.0	12	Invisible	−1.02	460	33	4
04295+2251.....	2	4 29 32.2	22 51 07.0	10	Invisible	−0.48	7.4	0.64	2
04325+2402.....		4 32 31.6	24 02 08.0	10	Invisible	< −0.92	22	0.93	16
04361+2547.....	5	4 36 09.4	25 47 27.0	10	Invisible	−1.02	35	3.7[e]	15
04365+2535.....	1, 2	4 36 31.0	25 35 52.0	10	Invisible	−0.86	39	2.4	2
L1527	6	4 36 49.3	25 57 16.0	10	Invisible	< −0.47	73	2.1	16
FS Tau.....	7, 8	4 18 57.63	26 50 30.5	13	Visible	−0.42	<11	1.7	18
T Tau	7	4 19 04.21	19 25 05.4	13	Visible	−0.47	98	14	18
DG Tau	7, 8	4 24 01.01	25 59 35.5	13	Visible	−0.32	46	7.7	18
HL Tau	8, 9	4 28 44.42	18 07 36.2	13	Visible	−0.48	<460	7.3	18
GG Tau	7	4 29 37.2	17 25 22.0	14	Visible	−0.11	5.2	2.3	18
DL Tau	7	4 30 36.02	25 14 24.0	13	Visible	−0.14	<2.3	1.1	18

REFERENCES.—(1) Adams et al. 1987; (2) Myers et al. 1987; (3) Sargent et al. 1988; (4) Keene & Masson 1990; (5) Terebey et al. 1990; (6) Ladd et al. 1991a; (7) Beckwith et al. 1990; (8) Adams et al. 1990; (9) Sargent & Beckwith 1987; (10) IRAS Point Sources Catalog 1984; (11) Tamura et al. 1991; (12) Rodríguez et al. 1986; (13) Jones & Herbig 1979; (14) Rydgren et al. 1984; (15) Kenyon et al. 1990; (16) Kenyon et al. 1993; (17) Ohashi 1991; (18) Cohen, Emerson, & Beichman 1989.

[a] Infrared colors between 12 and 25 μm.

[b] *IRAS* flux densities at 100 μm.

[c] Infrared luminosities derived from *IRAS* data and near-infrared data.

[d] These sources do not have any optical counterpart on the POSS blue print, although they are associated with a faint optical feature on the POSS red print.

[e] We estimated the luminosity at far-infrared wavelengths in the manner described by Myers et al. 1987 and added it to the luminosity estimated by Kenyon et al. 1990, because Kenyon et al. used only near-infrared and *IRAS* data in estimating the luminosity of IRAS 04361+2547.

that weak-line T Tauri stars, which may represent a more aged population with respect to classical T Tauri stars, have disk truncation radii fairly far away from their stellar surfaces, as was suggested by the absence of accretion-related phenomena around them (Edwards, Ray, & Mundt 1993).

Formation and growing processes of circumstellar disks are, on the other hand, less well understood. This is mainly because the formation of disks proceeds in a stage prior to the T Tauri phase, namely, in the embedded protostar phase when protoplanetary disks, if they already exist, as well as stars are deeply enshrouded by extended envelopes of 1–10 $M_\odot$ (Myers, Linke, & Benson 1983; Benson & Myers 1989). It is difficult for single-dish telescopes with even the highest angular resolutions to directly observe deeply embedded circumstellar disks without being contaminated by their extended envelopes; we need interferometric observations, which can pick up only the embedded circumstellar disks by resolving out the extended envelopes. Although there are some interferometric observations of compact disks around embedded protostar candidates (e.g., L1551–IRS 5, Keene & Masson 1990; IRAS 16293−2426, Mundy et al. 1992), they are limited in number. It is thus necessary to proceed with an interferometric survey of circumstellar disks around embedded sources so that we can derive evolutionary information through comparative studies of the disk properties of protostar candidates and T Tauri stars.

In Paper I we compared the matter distribution within a diameter of 1000 AU around embedded sources with that of T Tauri stars, finding that T Tauri stars tend to have more of their mass distribution concentrated around the central stars as compact disks. In this paper we report results from our continued NMA survey, with emphasis on kinematical structure around each observed source, and discuss the evolution of circumstellar disks based on the survey results.

2. SAMPLE

Our sample consists of 19 low-mass protostellar *IRAS* sources associated with the Taurus molecular cloud complex. We focused our survey on sources in the Taurus molecular cloud because it produces new stars with masses in a relatively narrow range of 0.4–0.8 $M_\odot$ (Cohen & Kuhi 1979), which is especially important when we discuss evolution of circumstellar matter without the effect of stellar mass variation. It is also important that the cloud is located close to the solar system (140 pc; Elias 1978), and has been a source of plenty of accumulated data at various wavelengths.

There are 1164 *IRAS* point sources in the Taurus region with right ascension (1950) ranging from 4^h to 5^h and declination (1950) from +15° to +30° (Joint *IRAS* Science Working Group 1988). We selected the sample of optically invisible protostellar sources out of the 1164 sources using the following five criteria.

1. Sources are significantly detected at three or four wavelength bands, including 25 and 60 μm.

2. Sources are not cataloged or optically identified as known bright stars, late type stars, or galaxies.

3. Sources are characterized by a cool infrared color temperature, i.e., log [$F(12)/F(25)$] < 0.0 and log [$F(25)/F(60)$] < 0.3. This limits the sources to either embedded

objects or T Tauri stars (Beichman et al. 1986; Emerson 1988), excluding normal stars from the sample.

4. Sources have correlation coefficients of 99% or 100% at the *IRAS* bands with significant detection. This eliminates extended sources such as infrared cirrus (Beichman 1986).

5. Sources are not optically visible on the Palomar Observatory Sky Survey.

In total, of the 1164 sources, 13 optically invisible sources satisfied the above five criteria.

There were 25 T Tauri stars that satisfied the above criteria, with the exception of the fifth one in the catalog of Beckwith et al. (1990). We note that some T Tauri stars in multiple systems were identified as single *IRAS* sources because of the large *IRAS* beam. Among these, we included in our survey six T Tauri stars with large flux densities at submillimeter and millimeter wavelengths for comparison.

The 19 selected sources are listed in Table 1. The bolometric luminosity listed in the column (9) includes the contribution from near- and far-infrared wavelengths (see the references listed in col. [10]), except for IRAS 04191+1523, for which near-infrared contributions were not included because of the lack of available photometric data at near-infrared wavelengths.

While the six T Tauri stars are as luminous as the 13 invisible sources, the *IRAS* colors between 12 and 25 μm for the invisible sources are cooler than those for the six T Tauri stars (see col. [7] of Table 1). According to the studies of protostellar *IRAS* sources by Beichman et al. (1986), optically invisible sources with cooler *IRAS* colors are in a younger evolutionary phase than T Tauri stars; the invisible sources may be accreting protostars deeply embedded in molecular cloud cores. Hence, we will call the 13 optically invisible sources "protostar candidates." Previous studies suggested that, except for IRAS 04169+2702, IRAS 04191+1523, and IRAS 04325+2402, the selected sources show evidence of compact circumstellar disks (see the references listed in col. [2] of Table 1).

3. OBSERVATIONS

We observed the 19 sources with the Nobeyama Millimeter Array (NMA) in the 3 mm continuum and CS ($J = 2$–1) emissions simultaneously. The observational period extended over three years from 1989 December to 1992 May as listed in Table 2. We used SIS receivers, with their typical noise temperature of $\sim$200 K in double sideband (DSB) (Kawabe et al. 1990), followed by the fast Fourier transform (FFT) spectrocorrelator FX with 1024 velocity channels as a backend (Chikada et al. 1987). The continuum data were taken by averaging over 900–950 line-free channels of FX where the band characteristic was flat. The resultant bandwidth for the continuum observations was 280–300 MHz. The velocity resolution for the CS line observations was 0.96 km s^{-1}. The total number of baselines for each source varied from 20 to 60.

The phase and gain of the array were calibrated by frequent observations of 0420−014, whose flux density was estimated in the manner described in Paper I. The complex bandpass across the 1024 frequency channels was determined through 30–40 minute observations of 3C 84 or 3C 273. We CLEANed CS channel maps and continuum maps using the NRAO Astronomical Imaging Processing System (AIPS). The total integrated intensity maps of CS were made by summing up the channel maps. Natural weighting was applied to the u-v data in making maps, and the resultant spatial resolution was 2″.8–10″, as a geometrical mean, corresponding to 390–1400 AU at the distance of Taurus. The typical rms noise levels of the CS and continuum maps were 130 mJy beam^{-1} ($\Delta v \sim 0.96$ km s^{-1}) and 4 mJy beam^{-1}, respectively. Typical positional uncertainty of the obtained maps is $\lesssim$1″.

4. INDIVIDUAL SOURCES

The results of the survey are summarized in Table 3. The 3 mm continuum maps and the integrated intensity maps of CS ($J = 2$–1) are presented in Figures 1 and 2, respectively. Columns (3)–(8) in Table 3 have the following meanings.

Column (3): Total integrated intensity of the CS emission in Jy km s^{-1}. Upper limits are 3 σ values, which were estimated from the rms noise level of each map under the assumption that the emission would be pointlike with its velocity width less than one resolving channel. Errors are 1 σ values estimated from the rms noise level of each integrated intensity map by integrating it over the same solid angle as the detected emission.

Column (4): FWHM size of the CS emission in AU measured on total integrated intensity maps. For the maps with more than one CS condensation, the size of each condensation is listed.

Column (5): Total gas mass in $M_\odot$ estimated from total integrated intensity maps of CS.

Column (6): Total flux density of the 3 mm continuum emission in mJy. Upper limits are 3 σ values and errors are 1 σ, which were estimated from the rms noise level of each map by assuming that the emission would be pointlike.

Column (7): FWHM size of the 3 mm continuum emission in AU. Upper limits to the size of unresolved sources are the half-power beamwidth (HPBW) beam sizes.

Column (8): Total gas mass in $M_\odot$ estimated from the total flux density of the 3 mm continuum emission on the assumption of the gas-to-dust mass ratio of 100. The 3 σ upper limit values are given for the sources not detected in the continuum emission.

In estimating the gas mass from CS, we assumed an optically thin emission with the fractional abundance of CS of 10^{-9} with respect to H_2 (Linke & Goldsmith 1980) and a mean molecular weight of 2.4. Although the excitation temperature of CS was assumed to be 75 K in Paper I, this value was derived based on the shallowest possible temperature distribution [$T(r) \propto r^{-1/3}$; see Paper I] and should

TABLE 2

PERIOD OF OBSERVATIONS

Period	Observed Sources
1989 Dec–1990 May.....	L1489, 04108+2803, 04169+2702, 04239+2436, 04295+2251, L1551–IRS 5, 04361+2547, L1527, FS Tau, DG Tau, HL Tau, GG Tau, DL Tau
1990 Dec–1991 Mar	04191+1523, 04295+2251, 04325+2402, 04365+2535
1992 Jan–1992 May	04154+2823, 04248+2612, T Tau

TABLE 3

OBSERVATIONAL RESULTS WITH THE NMA

OBSERVED SOURCE (1)	OPTICAL APPEARANCE (2)	CS ($J = 2$–1) I_{CS} (Jy km s^{-1})[a] (3)	CS ($J = 2$–1) Size (AU)[b] (4)	CS ($J = 2$–1) M_{CS} ($M_\odot$) (5)	3 mm CONTINUUM F_ν (mJy)[a] (6)	3 mm CONTINUUM Size (AU)[b] (7)	3 mm CONTINUUM M_d ($M_\odot$) (8)
L1489	Invisible	5.6 ± 0.51	2000×1700	4.3×10^{-2}	<9.6		$<2.2 \times 10^{-2}$
04108+2803	Invisible	1.4 ± 0.31	2700×1200	1.1×10^{-2}	<21		$<4.7 \times 10^{-2}$
04154+2823	Invisible	<0.42			<15		$<4.4 \times 10^{-2}$
04169+2702	Invisible	2.6 ± 0.45	1600×1500, 2000×1200	2.0×10^{-2}	<14		$<3.2 \times 10^{-2}$
04191+1523	Invisible	0.80 ± 0.16	1400×1400	6.1×10^{-3}	<9.0		$<2.1 \times 10^{-2}$
04239+2436	Invisible	2.8 ± 0.39	2700×1700	2.1×10^{-2}	<12		$<3.2 \times 10^{-2}$
04248+2612	Invisible	1.7 ± 0.31	3800×1500, 1800×1100	1.3×10^{-2}	<12		$<3.4 \times 10^{-2}$
04295+2251	Invisible	<0.56			<21		$<2.8 \times 10^{-2}$
L1551–IRS 5	Invisible	15 ± 0.92	2300×1600	1.1×10^{-1}	131 ± 4.0	$<430 \times 360$	7.0×10^{-2}
04325+2402	Invisible	0.86 ± 0.12	1800×1400	6.5×10^{-3}	<9.2		$<2.1 \times 10^{-2}$
04361+2547	Invisible	$1.4+0.41$	2100×1500, 2100×1500	1.1×10^{-2}	<14		$<3.2 \times 10^{-2}$
04365+2535	Invisible	2.5 ± 0.25	1500×1500	1.9×10^{-2}	30 ± 3.8	$<940 \times 700$	6.8×10^{-2}
L1527	Invisible	11 ± 0.86	2600×2000	8.4×10^{-2}	<11		$<2.5 \times 10^{-2}$
FS Tau	Visible	<0.34			<11		$<4.1 \times 10^{-2}$
T Tau	Visible	<0.60			56 ± 10	$<550 \times 420$	1.0×10^{-1}
DG Tau	Visible	1.4 ± 0.19	1600×730	1.1×10^{-2}	57 ± 4.0	$<800 \times 770$	1.0×10^{-1}
HL Tau	Visible	1.5 ± 0.21	1200×850	1.1×10^{-2}	74 ± 4.0	$<530 \times 420$	1.5×10^{-1}
GG Tau	Visible	<0.44			41 ± 4.0	$<780 \times 670$	1.6×10^{-1}
DL Tau	Visible	<0.37			23 ± 4.0	$<1470 \times 880$	1.0×10^{-1}

[a] Upper limit values are 3 σ and errors are 1 σ.
[b] FWHM size.

be regarded as an upper limit. This upper limit is consistent with the highest dust temperature of $\sim$60 K observed around protostellar sources (Moriarty-Schieven et al. 1994). On the other hand, the steepest possible temperature distribution following $T(r) \propto r^{-1/2}$ gives the excitation temperature of 10 K as a lower limit. We then adopted 30 K for the excitation temperature of CS in this paper. Note that the gas masses estimated from CS should be regarded as lower limits, because we assumed optically thin CS emission and because extended CS emission was resolved out.

In estimating the gas (total) mass from the dust emission, we assumed a dust temperature of 120 K for L1551-IRS 5 (Keene & Masson 1990) and 30 K for the other protostar candidates. For the observed T Tauri stars, we referred to the dust temperature at the radius of 100 AU taken from previous works (Adams et al. 1990; Beckwith et al. 1990). We used the dust mass opacity at 3 mm of 5.0×10^{-3} cm^2 g^{-1}, which was estimated from the mass opacity at 400 μm (Keene, Hildebrand, & Whitcomb 1982) under the assumption that the opacity has power-law dependence on wavelength ($\kappa_\lambda \propto \lambda^{-\beta}$) with the power-law index β being equal to 1 (see Paper I). We used the same dust opacity for both protostar candidates and T Tauri stars, although the mass opacity for T Tauri disks might be larger than that for protostars because of possible grain growth (see the discussion in § 5.4). Details of the mass estimation are described in Paper I (see also Appendix A).

We show results of individual sources for eight newly observed sources in § 4.1. Results of the other 11 sources were described in Paper I. For the protostar candidates L1489, L1551–IRS 5, IRAS 04365+2535, and L1527, which show considerable structure and large velocity gradients in CS, we discuss detailed gas distribution and kinematics in § 4.2. In discussing the kinematics of the four sources, we adopted their systemic velocities (listed in Table 4) taken from the peak velocities of C^{18}O ($J = 1$–0) measured with the Nobeyama 45 m telescope (17″ resolution). Results and discussion of the survey are given in § 5.

4.1. *Newly Observed Sources*

4.1.1. *IRAS 04154+2823*

IRAS 04154+2823 is an optically invisible source located in the large complex of L1495. Neither CS nor continuum emission was detected from it with our sensitivity of 0.42 Jy beam^{-1} (3 σ) and 15 mJy beam^{-1} (3 σ) for the CS and continuum emissions, respectively. Its bolometric luminosity is 0.33 $L_\odot$ (Myers et al. 1987), which is the least among the sample, while its *IRAS* color measured between 12 and 25 μm is the warmest among the protostar candidates. These facts imply that this object may have a relatively small stellar mass or mass accretion rate.

4.1.2. *IRAS 04191+1523*

IRAS 04191+1523 is an optically invisible source with a bolometric luminosity of 0.48 $L_\odot$. The source is located at the peak of a ^{13}CO core of 0.34 pc × 0.28 pc in size. It is associated with a young molecular outflow with its dynamical timescale of $\sim 10^4$ yr (Ohashi 1991).

The CS emission was detected only at one velocity channel corresponding to the LSR velocity of 7.28 km s^{-1} at the angular resolution of 5″.9 × 5″.0. The 3 mm contin-

TABLE 4

SYSTEMIC VELOCITY OF EACH SOURCE

Source	V_{LSR} (km s^{-1})
L1489	6.8
L1551–IRS 5	6.2
04365+2535	6.1
L1527	5.7

NOTE.—This velocity is estimated by Gaussian fitting to C^{18}O ($J = 1$–0) profiles obtained with the Nobeyama 45 m telescope (Ohashi et al. 1995).

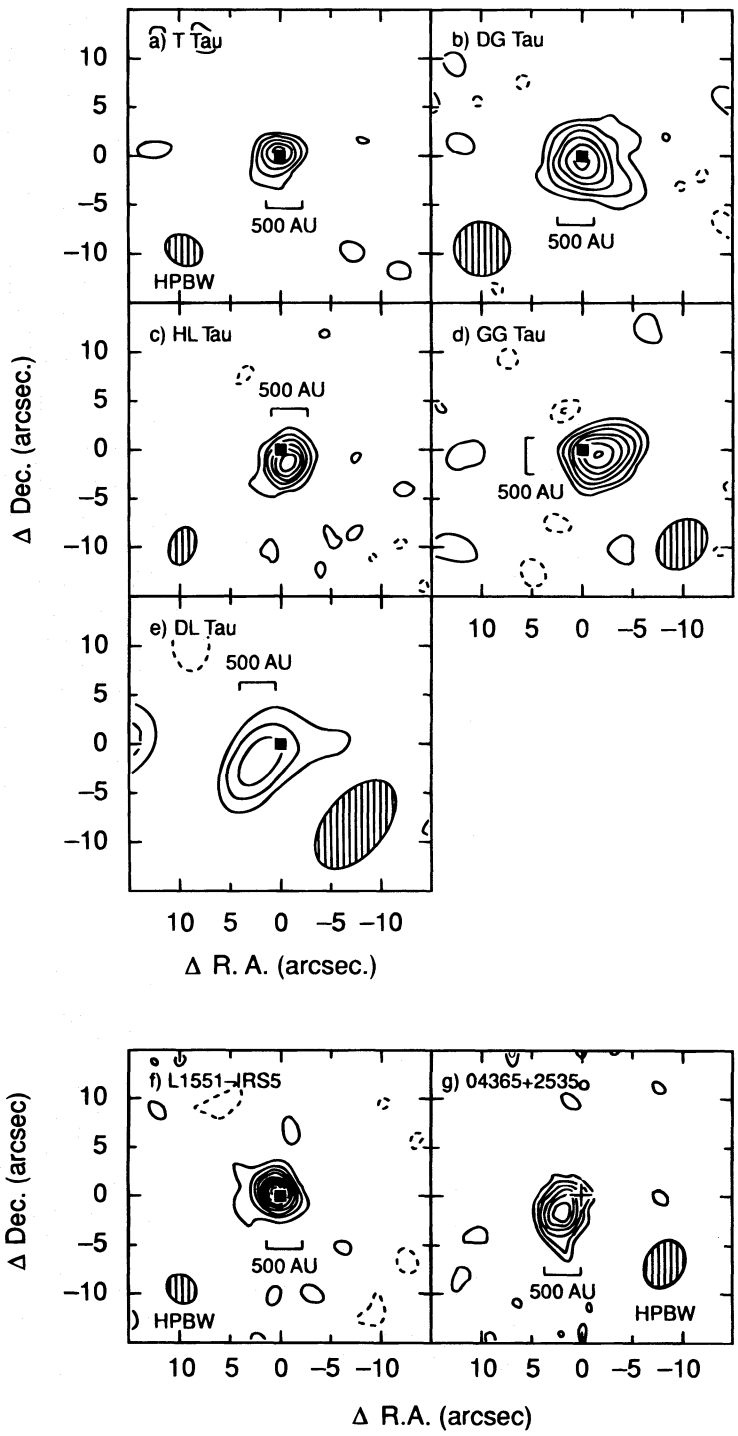

FIG. 1.—(*a–e*) 3 mm continuum maps of five T Tauri stars and (*f–g*) two protostar candidates. Synthesized beam size with its position angle for each source is indicated by a hatched ellipse in each panel. The contour interval for HL Tau and L1551–IRS 5 is 2 σ, with the positive contours starting from the 2 σ level (*solid line*) and with negative contours decreasing from the 2 σ level (*dashed line*). For the other sources, contours are drawn every 1 σ. Filled squares in panels (*a–f*) represent optical positions of T Tauri stars (Jones & Herbig 1979) and the 2 cm radio continuum position of L1551–IRS 5 (Rodríguez et al. 1986), respectively. The cross in panel (*g*) indicates the position of the 2.2 μm source, with its size showing the positional accuracy of $\pm 3''$ (Tamura et al. 1991).

uum emission was not detected with the sensitivity limit of 9.0 mJy beam^{-1} (3 σ). The CS map in Figure 2*d* shows a single condensation with the FWHM size of 1400 AU × 1400 AU. The 2.2 μm infrared source detected by Tamura et al. (1991) is coincident with the CS condensation within the positional uncertainties of the infrared and interferometric measurements. The CS condensation may therefore be dense circumstellar gas in the vicinity of the central infrared source. The total flux of the CS emission was 0.80 Jy km s^{-1}, which was converted to the total gas mass of $6.1 \times 10^{-3}\ M_{\odot}$ in the condensation.

4.1.3. *IRAS 04239+2436*

IRAS 04239+2436 is an optically invisible source with a bolometric luminosity of 1.2 $L_{\odot}$ (Kenyon, Calvet, & Hartmann 1993) embedded in a dense core of 33 mag in A_v

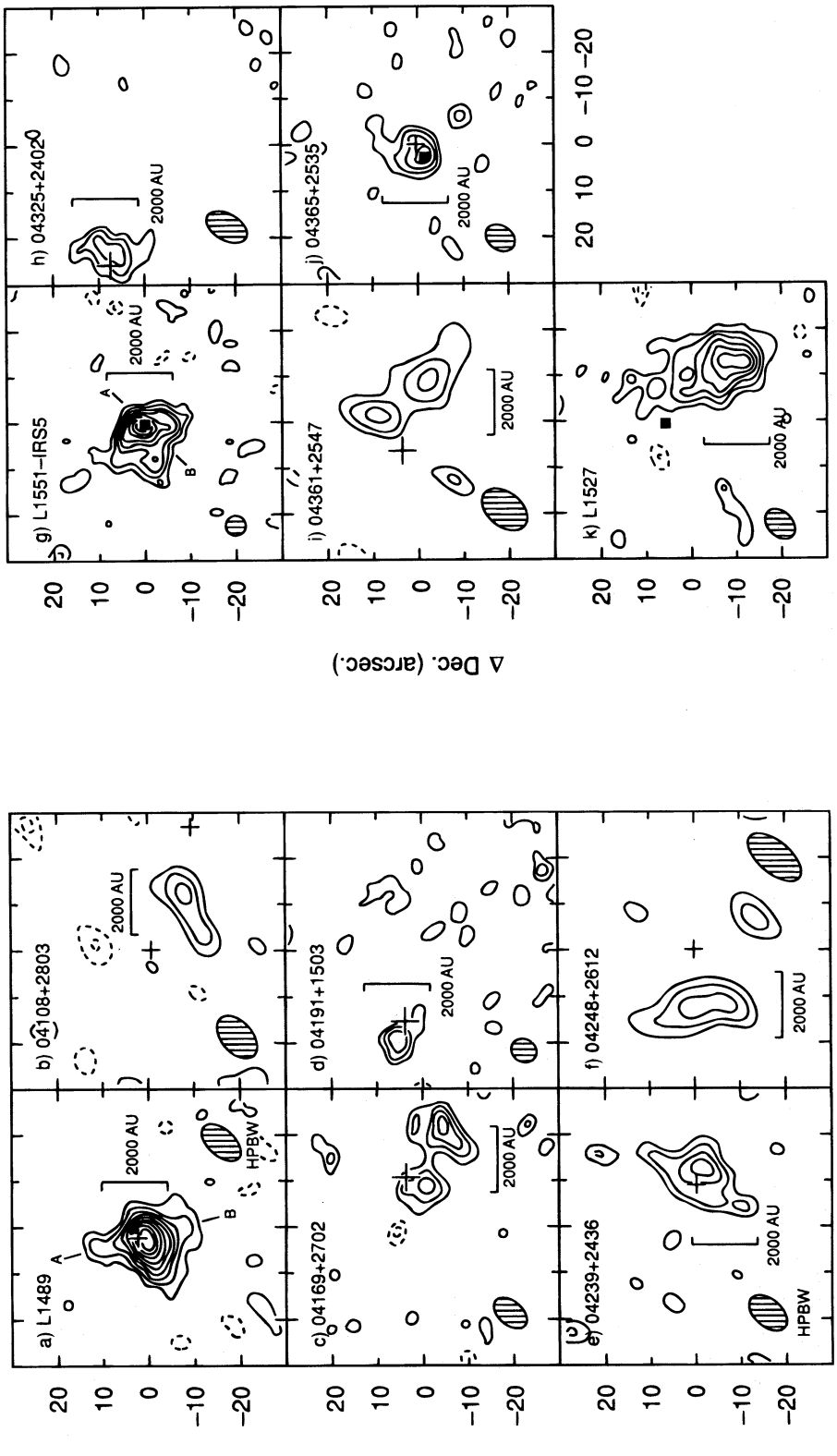

FIG. 2.—(*a–k*) Integrated intensity maps of CS ($J = 2–1$) for 11 protostar candidates and (*l–m*) T Tauri stars, with hatched ellipses showing each synthesized beam size and its position angle. Contours are drawn every 1 σ, with the positive contours starting from 2 σ level (*solid line*) and the negative contours decreasing from the -2 σ level (*dashed line*). Crosses in panels (*a–f*) and (*h–j*) mark positions of 2.2 μm sources, with their sizes showing positional accuracy (*small cross* $\pm 2''$; Myers et al. 1987; *large cross* $\pm 3''$; Tamura et al. 1991). (*a*) L1489. Integrated range is 5.84–9.68 km s^{-1} in LSR velocity. (*b*) IRAS 04108+2803. The CS emission is detected at one velocity channel, corresponding to $V_{LSR} = 6.32$ km s^{-1}, with $\Delta V = 0.96$ km s^{-1}. (*c*) IRAS 04169+2702. Integrated LSR velocity range is 6.80–8.72 km s^{-1}. (*d*) IRAS 0419+1523. CS emission was detected at $V_{LSR} = 7.28$ km s^{-1}, with a velocity resolution of 0.96 km s^{-1}. (*e*) IRAS 04239+2436. The map was integrated over the velocity range 5.84–8.72 km s^{-1}. (*f*) IRAS 04248+2612. The CS emission was detected at one velocity channel corresponding to $V_{LSR} = 7.28$ km s^{-1} with $\Delta V = 0.96$ km s^{-1}. (*g*) L1551-IRS 5. The integrated range is 3.92–9.68 km s^{-1} in LSR velocity. The square shows the position of the 2 cm radio continuum source (Rodriguez et al. 1986). (*h*) IRAS 04325+2402. The emission was detected at 8.24 km s^{-1} with $\Delta V = 0.96$ km s^{-1} in LSR velocity. (*i*) IRAS 04361+2547. The integrated LSR velocity range is 6.80–8.72 km s^{-1}. (*j*) IRAS 04365+2535. The integration range is 4.88–6.80 km s^{-1} in LSR velocity. The square shows the position of the 3 mm continuum source detected in this work. (*k*) L1527. The map was integrated over the LSR velocity range of 2.96–7.76 km s^{-1}. The square shows the 2 mm continuum position (Ohashi et al. 1995). (*l*) DG Tau. The integration range is 4.88–6.80 km s^{-1} in LSR velocity. The optical position of DG Tau is indicated by the filled square (Jones & Herbig 1979). (*m*) HL Tau. The integration range is 5.84–7.76 km s^{-1} in LSR velocity. The optical position of HL Tau is indicated by the filled square (Jones & Herbig 1979).

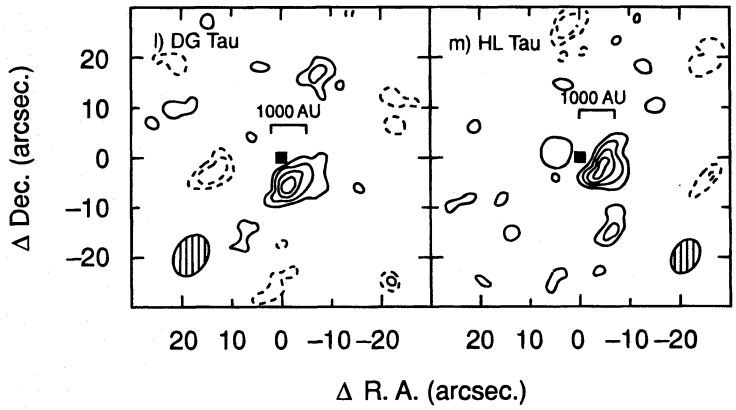

FIG. 2—*Continued*

(Myers et al. 1987). The continuum flux density steeply increases with wavelength between 0.4 and 100 μm.

We detected the CS emission from IRAS 04239+2436 with a spatial resolution of 9.″9 × 6.″0, while the 3 mm continuum emission was not detected with the sensitivity of 12 mJy beam^{-1} (3 σ). Figure 2*e* shows the CS map integrated over the velocity range of 5.84–8.72 km s^{-1}. The CS map has one condensation 2700 AU × 1700 AU in size (FWHM). It is elongated from northwest to southeast and slightly to the west. The 2.2 μm infrared source detected by Myers et al. (1987) is located near the CS peak, which implies that the CS gas is the circumstellar gas associated with the infrared source. The total flux of the CS emission was 2.8 Jy km s^{-1}, and the total gas mass contained in the condensation was 2.1 × 10^{-2} $M_\odot$.

4.1.4. *IRAS 04248+2612*

IRAS 04248+2612 is an optically invisible source with a bolometric luminosity of 0.35 $L_\odot$ (Kenyon et al. 1993). The source is located at the northeastern edge of the NH_3 core (B217) of 0.07 pc in radius (Benson & Myers 1989).

We detected CS emission from IRAS 04248+2612 at one velocity channel corresponding to the LSR velocity of 7.28 km s^{-1} with the resolution of 14.″2 × 7.″0. The 3 mm continuum emission was not detected with the sensitivity of 12 mJy beam^{-1} (3 σ). Figure 2*f* shows the CS map at the detected channel. We identified two CS condensations on the map: one was located to the east of the central source detected at 2.2 μm (Myers et al. 1987), and the other to the southwest of it. The eastern condensation is 3800 AU × 1500 AU in size (FWHM) with the elongation from north to south. The southwestern condensation, which is weaker than the eastern one, is 1800 AU × 1100 AU in size (FWHM). Both condensations are separated away from the central source by ~10″. The total flux of the CS emission is 1.7 Jy km s^{-1}, corresponding to the total gas mass of 1.3 × 10^{-2} $M_\odot$ in the CS condensations

4.1.5. *IRAS 04295+2251*

IRAS 04295+2251 is an optically invisible source with a bolometric luminosity of 0.64 $L_\odot$ (Myers et al. 1987). We detected neither CS nor continuum emission from this source with the sensitivity of 0.56 Jy beam^{-1} (3 σ) and 21 mJy beam^{-1} (3 σ) for the CS and continuum emissions, respectively. The ^{13}CO (J = 1–0) observations with the Nagoya 4 m radio telescope showed that there was no clear ^{13}CO core around IRAS 04295+2251 (Ohashi 1991). Recent observations of H^{13}CO$^+$ (J = 1–0) with the Nobeyama 45 m telescope did not show a clear molecular cloud core in its vicinity, either (Mizuno et al. 1994). These results as well as the *IRAS* characteristics of this object are similar to IRAS 04154+2823, which had the lowest luminosity and relatively warm color among the sample, and was not detected in either CS or continuum. This may suggest, as was the case for IRAS 04154+2823, that IRAS 04295+2251 has an intrinsically small stellar mass or mass accretion rate.

4.1.6. *IRAS 04325+2402*

IRAS 04325+2402, an optically invisible source with a bolometric luminosity of 0.93 $L_\odot$ (Kenyon et al. 1993), is located at the peak of a ^{13}CO core 0.8 pc × 0.4 in size (Ohashi 1991). This source has an extended molecular outflow with only its redshifted lobe observed (Heyer et al. 1987).

We detected CS emission from IRAS 04325+2402 at one velocity channel of 8.24 km s^{-1} with the resolution of 9.″7 × 5.″8, while the 3 mm continuum emission was not detected with the present sensitivity of 9.2 mJy beam^{-1} (3 σ). The CS map shown in Figure 2*h* has one condensation of 1800 AU × 1400 AU in FWHM size, with its peak coincident with a 2.2 μm source (Tamura et al. 1991). The observed CS emission is thus the circumstellar dense gas directly associated with the central source. The total flux of the CS emission was 0.86 Jy km s^{-1}, which was converted to the total gas mass of 6.5 × 10^{-3} $M_\odot$.

4.1.7. *IRAS 04365+2535*

IRAS 04365+2535 is an optically invisible source with a bolometric luminosity of 2.4 $L_\odot$ (Myers et al. 1987). It is located at the center of an NH_3 core (L1543) 0.14 pc in radius (Benson & Myers 1989). A theoretical model fitting its spectral energy distribution suggested its association with a circumstellar disks (Adams, Lada, & Shu 1987). A 2.2 μm source was detected toward the *IRAS* source (Myers et al. 1987). A recent outflow survey with the Nobeyama 45 m telescope and with the NMA revealed that this source exhibits a young CO outflow with its dynamical timescale of 2.5 × 10^3 yr (Hirano et al. 1995; see also Tamura et al. 1994).

We detected both continuum and CS emissions toward IRAS 04365+2535. Figure 1*g* shows the continuum map at the resolution of 7.″1 × 5.″2. The emission size was so compact as to be spatially unresolved at the present resolution. The peak position of the continuum emission derived through Gaussian fitting was R.A. (1950) = 4^{h}36^{m}31^s.2 and decl. (1950) = 25°35′54″. Although this position is shifted by ~3″ to the southeast of the 2.2 μm source,

this discrepancy probably results from the positional uncertainty of the 2.2 μm source ($\pm 2''$). We refer the continuum position to the central source position for IRAS 04365+2535 in this paper. The total flux density of the continuum emission was 30 mJy, corresponding to $6.8 \times 10^{-2}\ M_\odot$ in total gas mass.

Figure 2*j* shows the integrated intensity map of the CS emission at the spatial resolution of $7''.1 \times 5''.3$. The integration range is from 4.88 to 6.80 km s^{-1}. The CS map has a single condensation whose size is 1500 AU × 1500 AU in FWHM, with its peak position well coincident with the 3 mm continuum peak. The CS emission shows velocity structure, which will be discussed in § 4.2.3. The total flux of the CS emission was 2.5 Jy km s^{-1}, which was converted to the total mass of $1.9 \times 10^{-2}\ M_\odot$ contained in the condensation.

4.1.8. *T Tauri (IRAS 04190+1924)*

T Tauri (IRAS 04190+1924) is a well-known T Tauri star located at the peak of a ^{13}CO molecular cloud core (Ohashi 1991). Radio and infrared observations showed that T Tauri is a triple system (Dyck, Simon, & Zuckerman 1982; Schwartz, Simon, & Campbell 1986). Its spectral energy distribution is flat between 1 and 100 μm, and is well fitted by a disk model with a radius and mass of 120 AU and 0.1 $M_\odot$, respectively (Adams et al. 1990). Maihara & Kataza (1991), on the other hand, explained the flat spectral energy distribution in terms of the composite spectrum of stars in the triple system.

We detected 3 mm continuum emission from T Tauri with the resolution of $3''.9 \times 3''.0$, while CS emission was not detected with the present sensitivity of 0.60 Jy beam^{-1}. In the continuum map shown in Figure 1*a*, the emission is not resolved at the present resolution, which means that the extent of the continuum emission is significantly smaller than 550 AU × 420 AU in FWHM. The peak of the continuum emission is coincident with the optical position of T Tauri. These results suggest that the observed continuum emission arises from the circumstellar disk around T Tauri.

The total flux density of the 3 mm continuum from T Tauri was 56 mJy, which is consistent with the spectral energy distribution of T Tauri from millimeter to submillimeter wavelengths with its spectral index of 2.0 (Beckwith & Sargent 1991). If the detected continuum emission is entirely due to dust emission from the circumstellar disk, the disk mass is estimated to be 0.10 $M_\odot$, under the assumption of the dust temperature of 36 K. This mass is ~6 times larger than that estimated from the flux density measured at 1.3 mm (Beckwith et al. 1990), which was caused because we used a different mass opacity as well as assumed a optically thin disk with a single temperature (see Appendix A for details). Possible contamination of free-free emission to the 3 mm flux density is discussed in Appendix B.

4.2. *Kinematics of* CS *Gas*

4.2.1. *L1489 (IRAS 0416+2610)*

The total integrated intensity map of CS presented in Figure 2*a* shows a centrally condensed peak with extended emission elongated from north to south by ~3000 AU with the position angle of ~15°. The elongated structure is symmetric with respect to the 2.2 μm source (Myers et al. 1987) and is roughly perpendicular to the axis of the molecular outflow defined by the eastern blueshifted and western redshifted lobes (Myers et al. 1988). Infrared images of L1489 showed that infrared reflection nebulosity is also elongated to the east of the 2.2 μm source, suggesting that the outflow direction at small scales is also in the east-west direction (Emerson & Moore 1995). Being perpendicular to the outflow direction, the elongated structure from north to south observed in CS may therefore be a gaseous disk of ~1500 AU in radius surrounding the central source.

Figure 3 shows the velocity channel maps of CS. The emission is significantly detected at three velocity channels centered on 6.32 km s^{-1} (Fig. 3*b*), 7.28 km s^{-1} (Fig. 3*c*), and 8.24 km s^{-1} (Fig. 3*d*), with additional emission marginally detected at 9.20 km s^{-1} (Fig. 3*e*). The peak of the CS emission at 6.32 km s^{-1}, which is slightly blueshifted with respect to the systemic velocity of 6.8 km s^{-1} (see Table 4), coincides with the central infrared source, although the emission peak is offset slightly to the southeast from it. The CS emission at this velocity is elongated to the northwest. At 7.28 km s^{-1}, the CS emission peaks at ~4″ to the southeast of the infrared source with weaker extension toward the north. The CS peak at 8.24 km s^{-1} is located ~3″ to the southwest of the central source with the extended emission elongated toward the south from the peak. While the emission peak moves from east to west with velocity, the extended weaker emission, which may be a disk as pointed out above, has an overall velocity gradient from north to south suggestive of rotation of the gas disk. This can also be seen in Figure 4 in which we presented a position-velocity diagram along the cut A-B drawn in Figure 2*a*. The CS emission has a clear velocity shift between its northern and southern parts with large velocity width observed at the position of the infrared source. The shift of the emission peak positions from east to west with velocity, on the other hand, has the same sense as the bipolar outflow and might be due to the outflow. We must be careful, however, that we would observe the same velocity pattern when the CS peak traces the near and far sides of an infalling gas disk seen nearly edge-on, as was observed for HL Tau (Hayashi, Ohashi, & Miyama 1993). We cannot tell at this point whether the velocity shift of the CS peak represents an infalling gas disk or part of the outflow, because the spatial and velocity resolutions are still too low and the exact outflow direction is ambiguous at this spatial scale.

4.2.2. *L1551–IRS 5 (IRAS 04281+1801)*

The integrated intensity map of CS toward L1551–IRS 5 presented in Figure 2*g* shows a peak coincident with the 2 cm radio continuum source (Rodríguez et al. 1986). The emission is elongated from north to south at higher level contours, while extending toward the northeast and east at lower levels. The channel maps of CS in Figure 5 show that strong CS emission is detected at 6.32 and 7.28 km s^{-1} and the emission gets weaker at 5.36 and 8.24 km s^{-1}. There are two emission features outside the HPBW primary field: one is located ~40″ northeast of L1551–IRS 5 at 5.36 km s^{-1}, and the other ~25″ west of it at 7.28 km s^{-1}. Although they might be real features, we do not discuss them because they are located outside the HPBW primary field. At the most blueshifted velocity of 5.36 km s^{-1}, a weak peak is coincident with the central source with an additional weak one located ~10″ to the south. At the velocity channel of 6.32 km s^{-1}, which includes the systemic velocity (see Table 4), the peak emission occurs ~6″ to the south of the central

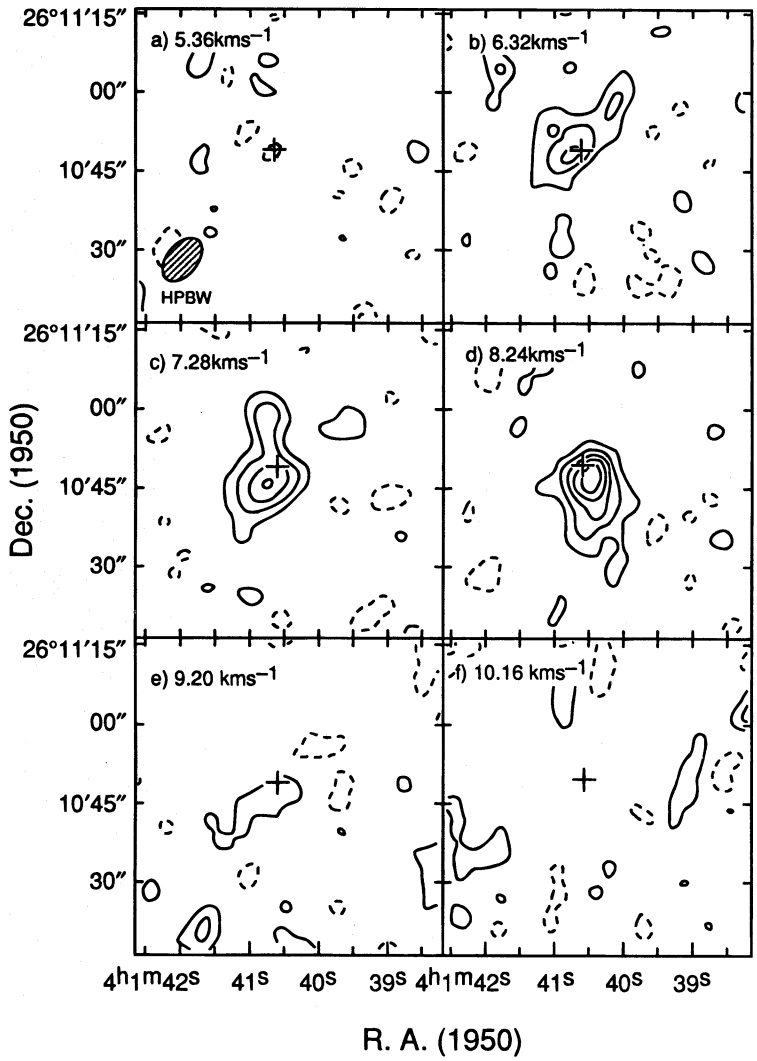

FIG. 3.—CS velocity channel maps of L1489 with the corresponding LSR velocity noted in the upper left-hand corner of each panel. Contours are drawn every 1.5 σ, with the positive contours starting from the 1.5 σ level (*solid line*) and with negative contours decreasing from the -1.5 σ level (*dashed line*). The cross in each panel and the hatched ellipse have the same meanings as in Fig. 2*a*.

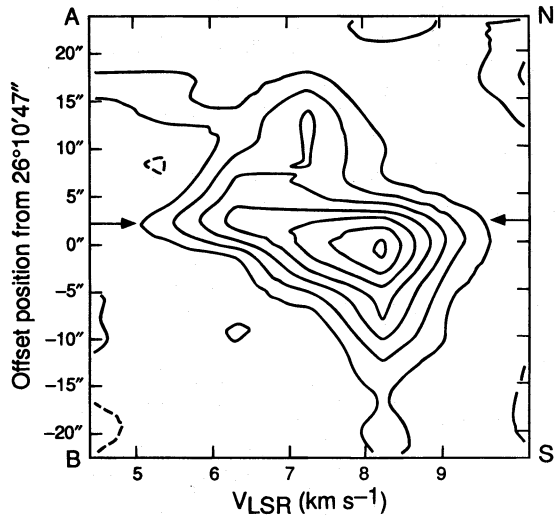

FIG. 4.—Position-velocity diagram of CS from L1489 cutting along the line A-B indicated in Fig. 2*a*. Contour levels are the same as in Fig. 3. The position of the 2.2 μm source (Myers et al. 1987) is indicated by arrows.

source with weaker extended emission. At the redshifted channel of 7.28 km s^{-1}, the CS emission has the strongest peak coincident with the central source, while exhibiting weaker extended emission elongated toward the northeast from the peak. At the most redshifted channel of 8.24 km s^{-1}, a weak CS peak is located $\sim 5''$ northeast of the central source and another $\sim 12''$ east.

While the detailed velocity field is complicated, the major velocity gradient is from south to north across the central source. Although this sense of velocity gradient is consistent with that observed by Kaifu et al. (1984) and Sargent et al. (1988), the gradient cannot easily be attributed to the rotation of a gas disk around L1551–IRS 5. We show a position-velocity diagram in Figure 6 along the line with its position angle of $\sim 135°$ (the line A-B in Fig. 2*g*), which is the direction of the major axis of the $C^{18}O$ rotating disk observed by Sargent et al. (1988). Figure 6 implies that there is no clear evidence of apparent rotation along the disk plane perpendicular to the bipolar outflow. Thus, the velocity gradient seen in CS ($J = 2$–1) may rather be attributed

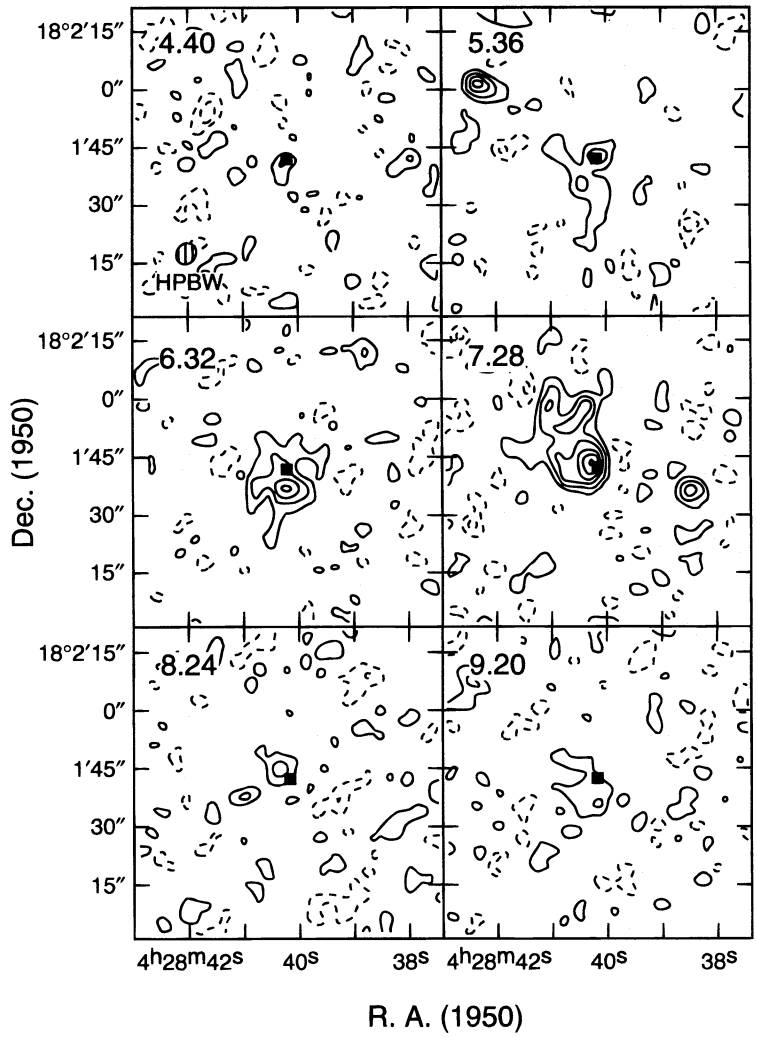

FIG. 5.—CS velocity channel maps of L1551–IRS 5 with the corresponding LSR velocity noted in the upper left-hand corner of each panel. Contours are drawn every 1.5 σ with the positive contours starting from the 1.5 σ level (*solid line*), and with negative contours decreasing from the -1.5 σ level (*dashed line*). A filled square in each panel and the hatched ellipse have the same meanings as in Fig. 2*g*.

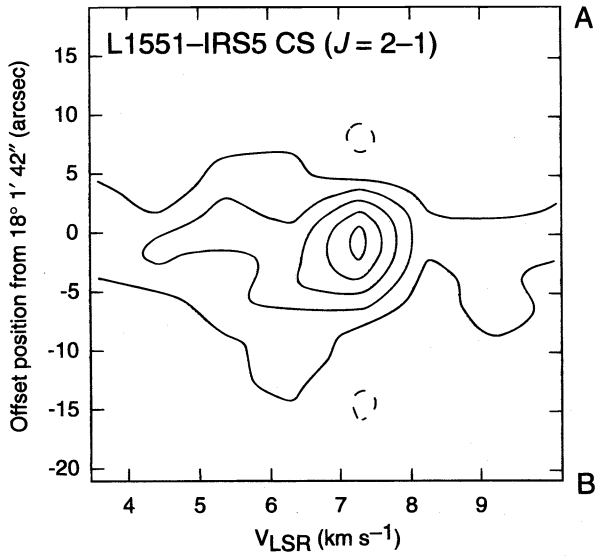

FIG. 6.—Position-velocity diagram of CS from L1551–IRS 5 cutting along the line A-B indicated in Fig. 2*g*. Contours are drawn in the same manner as in Fig. 5.

to the bipolar outflow or to the infall of the disk as in the case for L1489 (see § 4.2.1). It may be rather clear that extended weak emission features such as the one extended to the northeast of IRS 5 at 7.28 km s^{-1} are denser regions of molecular outflows, as evidenced by its fan-shaped morphology and blueshifted velocity. The velocity field of the compact emission as traced by higher level contours at each velocity channel is rather difficult to understand at the present resolution and quality of data, and we must await further observational data. We note that $C^{18}O$ ($J = 1$–0) observations with the NMA have detected possible infalling motion around IRS 5 (Ohashi et al. 1996). We also note that recent NMA observations of CS ($J = 3$–2), which traces much higher density, have revealed more compact structure around IRS 5 suggestive of both rotation and infall of the circumstellar disk (Kawabe et al. 1996).

4.2.3. *IRAS 04365+2535*

Figures 7*a* and 7*b* show the CS maps toward IRAS 04365+2535 at the two detected velocity channels, and Figure 7*c* is the total integrated intensity map. The CS emission was detected at 6.32 km s^{-1}, which includes the sys-

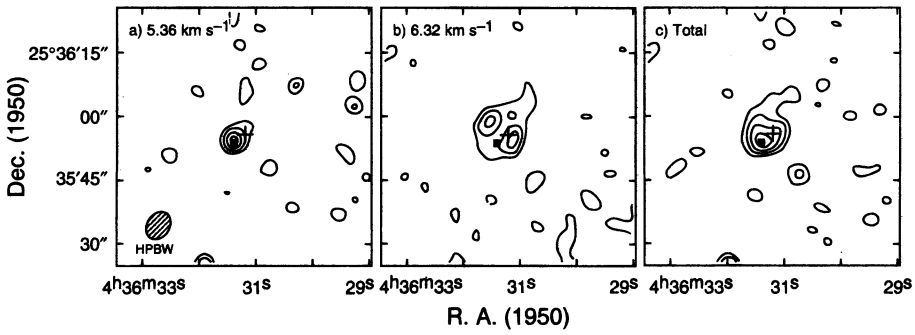

FIG. 7.—CS velocity channel maps of IRAS 04365+2535, with the corresponding LSR velocity noted in the upper left-hand corner of panels (*a*) and (*b*), and (*c*) its integrated intensity map. Contours of the channel maps are drawn every 1.5 σ with the positive contours starting from the 1.5 σ level (*solid line*), and with negative contours decreasing from the -1.5 σ level (*dashed line*). Contour levels of the integrated intensity map are the same as in Fig. 2*j*. A cross and a square in each panel and the hatched ellipse have the same meanings as in Fig. 2*j*.

temic velocity (6.1 km s^{-1}; see Table 4), and at 5.36 km s^{-1}. No significant CS emission was detected at redshifted velocities. The emission at 5.36 km s^{-1} has a single peak well coincident with the continuum peak, which is assumed to be the true position of the central source in this paper (see § 4.1.7). The 6.32 km s^{-1} component has two peaks: one $\sim$5" to the northeast and the other $\sim$5" to the west of the central source.

Figure 8 shows the CS emission at 6.32 km s^{-1} superimposed on the blueshifted and redshifted lobes of the molecular outflow observed by Tamura et al. (1994) with NMA. The two CS peaks are located symmetrically with respect to the ridges of the blueshifted and redshifted outflow lobes and aligned perpendicular to the outflow axis. Such morphology suggests that the two peaks correspond to the outer regions of a disk or a ring that surrounds the central source. The radius of the disk or ring structure is estimated to be $\sim$500 AU.

The origin of the CS emission at 5.36 km s^{-1} is not clear. It may be the inner part of the disk with higher radial or rotational velocities, or it may be the denser part of the blueshifted outflow. The momenta carried with the blueshifted CS and CO components are consistent with each other as is compared in Table 5. This might suggest the possibility that the blueshifted CS is part of the outflow.

4.2.4. *L1527 (IRAS 04368+2557)*

The integrated intensity map of CS toward the protostellar source IRAS 04368+2557 embedded in L1527 is shown in Figure 2*k*, where the filled square is the position of a compact 2 mm continuum source at R.A. (1950) = 4^{h}36^{m}49^s.5 and Decl. (1950) = 25°57'21" recently detected with NMA (Ohashi et al. 1995). Because the continuum peak is well coincident with that observed at submillimeter wavelengths (Ladd et al. 1991b), we hereafter regard the 2 mm continuum position as that for the central energy source. Figure 2*k* shows that no CS emission was detected at the position of the central source, while one strong and one marginal CS condensation were detected at the west

TABLE 5

MOMENTA OF THE BLUESHIFTED CS GAS AND THE BLUESHIFTED CO OUTFLOW FOR IRAS 04365+2535

Emission Line	Velocity (km s^{-1})	Mass ($M_\odot$)	Momentum[a] ($M_\odot$ km s^{-1})	Reference
CS.....	5.36	9.2×10^{-3}	6.8×10^{-3}	1
CO	-2.96–5.14	1.1×10^{-3}	3.9×10^{-3}	2

[a] We adopted 6.1 km s^{-1} as the systemic velocity of the ambient cloud associated with IRAS 04365+2535.

REFERENCES.—(1) This work; (2) Tamura et al. 1994.

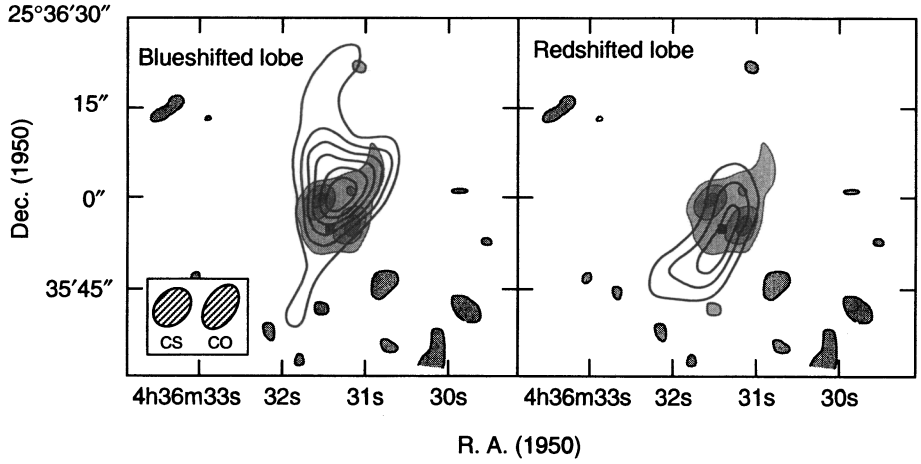

FIG. 8.—CS velocity channel map of IRAS 04365+2535 at V_{LSR} = 6.32 km s^{-1} in gray scale superposed on CO (J = 1–0) outflow maps observed with NMA (Tamura et al. 1995): (*left panel*) blueshifted lobe, (*right panel*) redshifted lobe. Contours of the outflow maps are drawn from the 3 σ level every 1.5 σ. Synthesized beam sizes of the CS and CO maps are shown by hatched ellipses. The position of the 3 mm continuum source is indicated by a square in each panel.

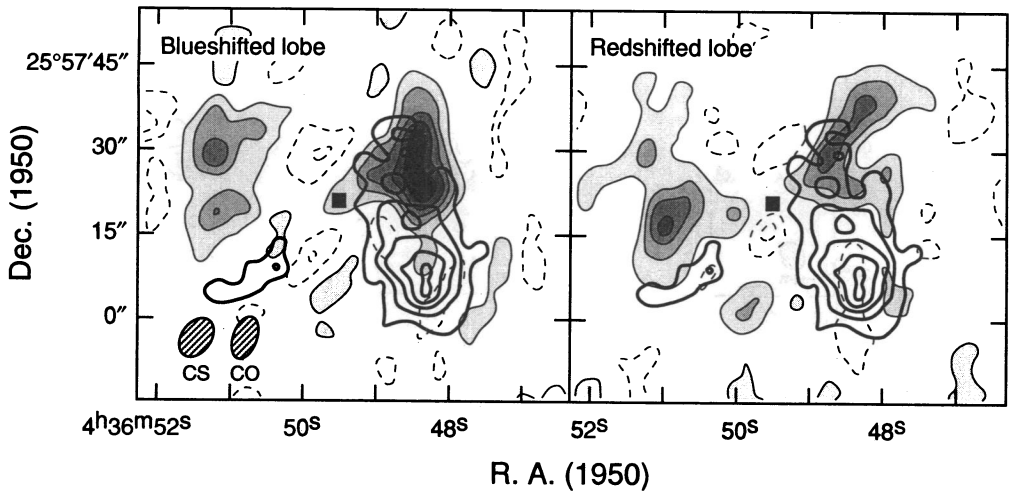

FIG. 9.—CS integrated intensity map of L1527 presented in Fig. 2*k* drawn in thick contours superposed on CO ($J = 1$–0) outflow maps in thin contours with gray scale observed with NMA (Tamura et al. 1995): (*left panel*) blueshifted lobe, (*right panel*) redshifted lobe. Contours of the outflow maps are drawn every 1.5 σ, with the positive contours starting from 1.5 σ level (*solid line*) and with negative contours decreasing from the -1.5 σ level (*dashed line*). Synthesized beam sizes of the CS and CO maps are shown by hatched ellipses. A square in each panel has the same meaning as in Fig. 2*k*.

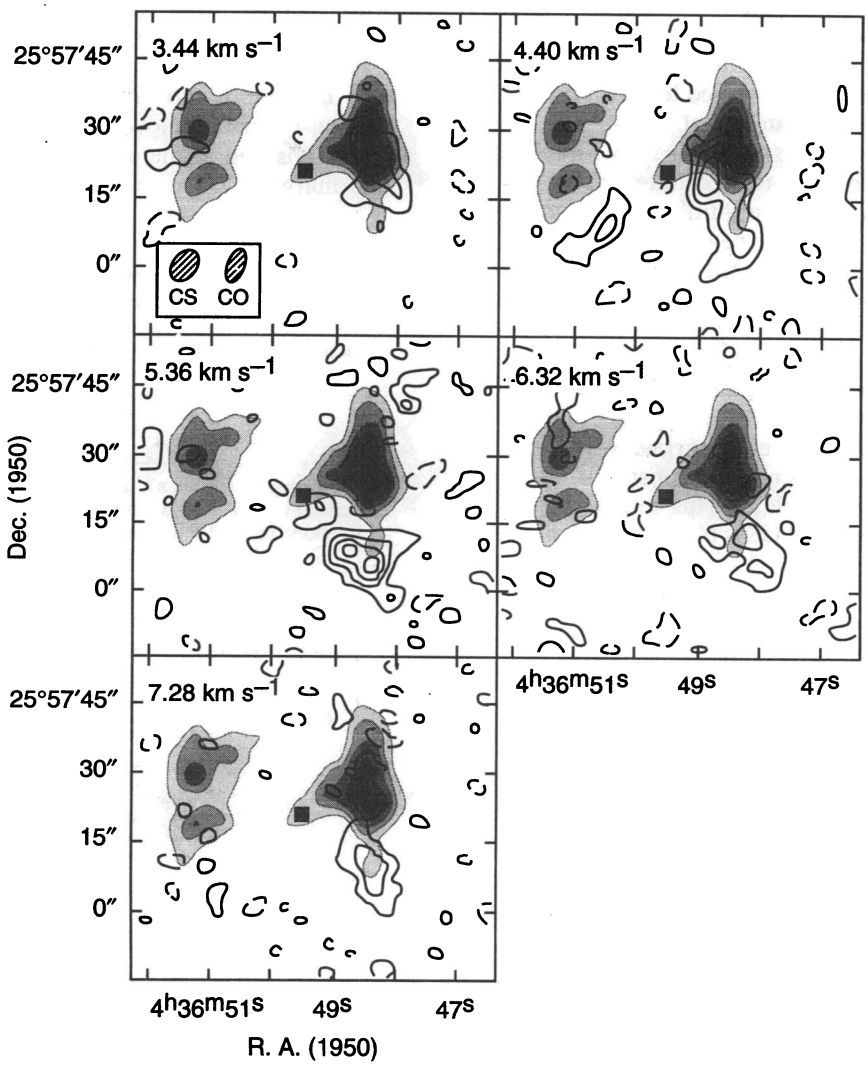

FIG. 10.—CS velocity channel maps of L1527 drawn in thick contours superposed on the CO blueshifted outflow map in gray scale presented in Fig. 9. Contours of the CS channel maps are drawn every 1.5 σ, with the positive contours starting from 1.5 σ level (*solid line*) and with negative contours decreasing from the -1.5 σ level (*dashed line*). A square in each panel and two hatched ellipses have the same meanings as in Fig. 9.

TABLE 6

MOMENTA OF THE WESTERN CS CONDENSATION AND THE WESTERN CO OUTFLOW TOWARD L1527

Emission Line	Velocity (km s^{-1})	Mass ($M_\odot$)	Momentum[a] ($M_\odot$ km s^{-1})	Reference
CS.....	3.44–7.28	2.1×10^{-1}	2.4×10^{-1}	1
CO	3.52–8.38[b]	7.3×10^{-3}	1.1×10^{-2}	2

[a] We adopted 5.7 km s^{-1} as the systemic velocity of the ambient cloud associated with L1527.

[b] The CO outflow was not detected between 4.33 and 6.76 km s^{-1}.

REFERENCES.—(1) This work; (2) Tamura et al. 1995.

and the southeast of the central source, respectively. The western CS condensation is elongated by ~4000 AU from north to south with its peak located at the southwestern edge. The southeastern CS condensation also shows elongation. Being separated away from the central source by ~3000 AU, the strong CS condensation is not directly associated with the central source; this is different from the case for the other sources, where CS emissions were detected in the vicinity of or toward the protostar candidates.

In Figure 9 we compare the integrated intensity of CS with the CO outflow recently observed by Tamura et al. (1995) with NMA. Although the outflow morphology is bipolar, its velocity field does not show clear bipolarity. Both blueshifted and redshifted emissions have two main lobes: one located ~15″ east of the central source and the other ~10″ to the west or northwest of it. Moreover, the two blueshifted lobes well overlap the corresponding two redshifted lobes. Such an outflow configuration may naturally be expected when we observe the outflow whose axis is almost on the plane of the sky, which is consistent with the extremely high extinction toward this source because we would observe its surrounding gas disk edge-on (Ladd et al. 1991a).

Having a closer look at Figure 9, we notice that CO and CS are spatially anticorrelated with each other; the peak of the western CS condensation is located at the southern edge of the western CO lobe in each channel map, and the southeastern CS condensation delineates the southern edge of the eastern CO lobe. We show in Figure 10 a more detailed comparison of CS with the blueshifted outflow lobe of CO at each CS velocity. The CS emission was detected at velocity channels from 3.44 km s^{-1} to 7.28 km s^{-1}. While overlapping the western CO lobe at 4.40 km s^{-1}, the CS emission is located to the south of CO at other detected channels. Such an anticorrelated distribution between CS and CO would suggest that the CS emission arises from a dense swept-up shell surrounding the outflow. Similar dense shell structures surrounding molecular outflows were observed toward several other objects (e.g., NGC 2071, Kitamura, Kawabe, & Ishiguro 1992; L1287, Yang, Ohashi, & Fukui 1995; T Tauri, Momose et al. 1995). We should be careful, however, that the observed compact CO outflow does not have sufficient momentum to accelerate the CS gas. Table 6 compares the momentum of the western outflow with that of the western CS condensation, showing that the momentum of the CS condensation is 1 order of magnitude larger than that of the outflow. This would mean that the compact outflow observed by Tamura et al. (1995) is not sufficient to accelerate the CS gas, which might make the swept-up shell interpretation rather vague. We also note, however, that both CO and CS observations were made with NMA, which have resolved out much of the extended structures in CS and CO, so that we should not rely too much on simple momentum arguments. Recent single-dish observations have actually revealed that the outflow is more extended (Macleod & Avery 1995). Such extended outflow gas may have sufficient momentum to push the observed CS condensations.

5. RESULTS AND DISCUSSION

5.1. *The* 3 mm *Continuum Emission*

The 3 mm continuum emission was detected from two protostar candidates and five T Tauri stars as summarized in Table 7. Comparison of the total flux density at 3 mm with spectral energy distributions of the observed sources at centimeter, millimeter, and submillimeter regions reveals that, except for T Tau, the contribution of free-free emission to the 3 mm flux density is at most 30%, suggesting that most of the 3 mm flux density is due to thermal emission originating from dust grains. As shown in Figure 1, none of the detected continuum emissions was resolved at our spatial resolution of ~500 AU in radius. These results suggest that the 3 mm continuum emission most probably arises from dust particles located in compact circumstellar disks with radii much smaller than 500 AU. The masses of these circumstellar disks were estimated to be 0.068–0.16 $M_\odot$ under the assumption of the gas-to-dust mass ratio of 100. Note that the estimated masses depend on the assumed opacity of dust grains, as will be discussed in § 5.4.

Cabrit & André (1991) showed that young stellar objects with well-developed molecular outflow have much stronger 1.3 mm dust continuum emission. In our survey, two protostar candidates (L1551–IRS 5 and IRAS 04365+2535) with detectable 3 mm continuum emission have well-developed and strong molecular outflows (L1551–IRS 5, Snell, Loren, & Plambeck 1980; IRAS 04365+2535, Moriarty-Schieven et al. 1994; Hirano et al. 1995). However, the other protostar candidates associated with well-developed molecular outflows (L1489, Myers et al. 1988; IRAS 04191+1523, Ohashi 1991; L1527, Tamura et al. 1995; Macleod & Avery 1995) did not have detectable 3 mm continuum emission, although recent 2 mm observations showed that L1527 is associated with relatively weak continuum emission (~60 mJy at 2 mm; see also Terebey, Chandler, & André 1993). Our survey shows that well-developed outflow sources do not necessarily have strong dust continuum emission, while protostar candidates with strong and compact dust continuum emission are associated with well-developed molecular outflows.

5.2. *The* CS (J = 2–1) *Emission*

The CS (J = 2–1) emission was detected from 11 protostar candidates and two T Tauri stars (see Table 7 for a

TABLE 7

DETECTABILITY OF THE 3 mm CONTINUUM AND CS (J = 2–1) EMISSION

	Number of Detected Sources	
Source[a]	Continuum Emission	CS Line Emission
Invisible sources (13).....	2	11
Visible sources (6).....	5	2

[a] Parentheses enclose number of observed sources.

summary). The CS condensations around the observed sources are well resolved with their typical size of ~2000 AU (FWHM); the CS emission is extended compared to the 3 mm continuum.

Among the 11 embedded sources detected in CS, seven sources have a CS emission that is well coincident with infrared sources. The emission arises from inner portions of dense cores associated with the infrared sources. For the other four sources, the CS emission is separated away from known infrared sources, which means that the emission is not directly associated with the central sources but may originate from compact, dense gas close to them. The total gas mass contained in the observed CS condensations around the embedded protostar candidates was estimated to be between 6.1×10^{-3} and 1.1×10^{-1} $M_\odot$ from the total integrated intensity of the CS emission, which was assumed to be optically thin. These values should be interpreted as lower limits, because the CS emission is probably optically thick. We also note that the mass derived from CS is just the small fraction of the total gas mass gravitationally associated with the observed sources, because the CS emission extending more than 40″ (5600 AU) was completely resolved out even if the gas density is sufficiently high enough to excite the rotational levels of CS molecules.

For T Tauri stars, the CS emission was detected from HL Tau and DG Tau. Inspection of Figure 2, however, leads us to find that the CS condensations around HL Tau and DG Tau avoid the stellar positions; no CS emission was detected directly toward them. They tend to be smaller in size and weaker in intensity than those around the embedded protostar candidates. The CS condensations detected around the two T Tauri stars may then be partially dissipated remnants of gaseous envelopes or dense cores, from which the two stars have been formed.

The above results on CS are consistent with a generally believed evolutionary sequence that embedded protostars associated with molecular cloud cores evolve into T Tauri stars with remnant envelopes. Figure 11 shows the relation between the *IRAS* color measured between 12 and 25 μm and the integrated intensity of CS, demonstrating the difference in the CS detectability between the embedded protostar candidates and T Tauri stars. There is a clear trend that sources with warmer *IRAS* colors have smaller CS intensities. The trend implies the dissipation of dense cores as a result of protostellar evolution from protostars to T Tauri stars as pointed out above. This correlation is basically the same as that shown by Hayashi et al. (1994) between the $C^{18}O$ ($J = 1$–0) intensity and the *IRAS* color for young stellar objects in Taurus.

When we focus only on the protostar candidates in Figure 11, the correlation between the CS intensity and the *IRAS* color is not clear. Hence, there may be factors other than evolution that are essential for the CS intensity for the embedded sources. We then investigated the relation between the CS intensity and the bolometric luminosity in Figure 12. It shows that, among the sample of embedded protostar candidates, the CS intensity is correlated with the bolometric luminosity with a correlation coefficient of 0.81. Although the correlation is not very tight, it may suggest that more luminous protostar candidates are associated with more massive protostellar envelopes. One might note that the CS intensity would not be correlated with the total mass of protostellar envelopes, because the CS emission may be optically thick and much of the extended emission is resolved out. We show in Figure 13 that the CS intensity for protostar candidates is in fact correlated with the total mass of their envelopes measured by the *IRAS* flux density at either 100 or 60 μm, which is a good tracer of the total amount of matter around embedded sources (Beichman et al. 1986; Hayashi et al. 1994). We may therefore conclude that more luminous protostar candidates are associated with more massive envelopes. Because the luminosity of accreting protostars is proportional to the stellar mass and mass accretion rate ($L_{acc} = GM_* \dot{M}/R_*$; Stahler, Shu, & Taam 1980), high-luminosity sources have high stellar masses and mass accretion rates, which naturally result in large final stellar masses when accreting timescales do not change much among those sources. The correlation shown in Figure 12 qualitatively supports the possibility that massive cores form massive stars. Such a trend is consistent with the recent theory by Nakano, Hasegawa, & Norman (1995), who studied mechanisms of determining the stellar mass in the process of star formation, finding that the final stellar mass depends mainly on the mass of initial cloud cores when they are mainly dissipated away by outflows.

5.3. *Difference in the* 3 mm *Continuum Detectability*

Table 7 shows that the fraction of continuum detection among the protostar candidates is much lower than that

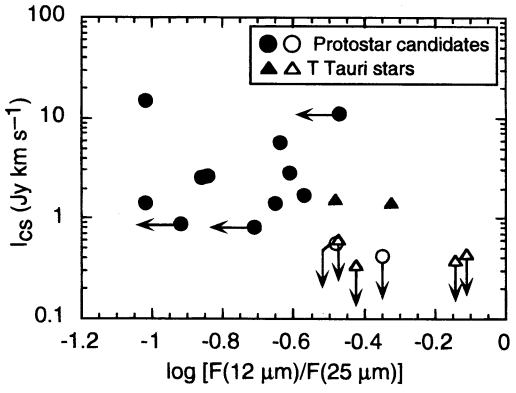

FIG. 11.—CS integrated intensities in Jy km s^{-1} toward all the observed sources are plotted as a function of infrared color between 12 and 25 μm. Upper limit values are indicated by arrows. Circles and triangles show protostar candidates and T Tauri stars, respectively. Open marks mean sources not detected in CS.

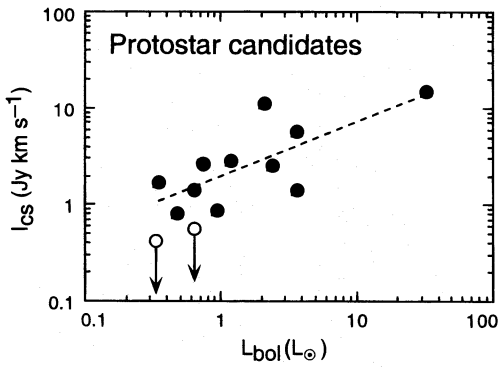

FIG. 12.—CS integrated intensities in Jy km s^{-1} toward all the 13 protostar candidates are compared with their bolometric luminosities. Open circles with an arrow indicate upper limits to integrated intensity. The dashed line shows the best fit to the detected 11 sources by a least-squares fit.

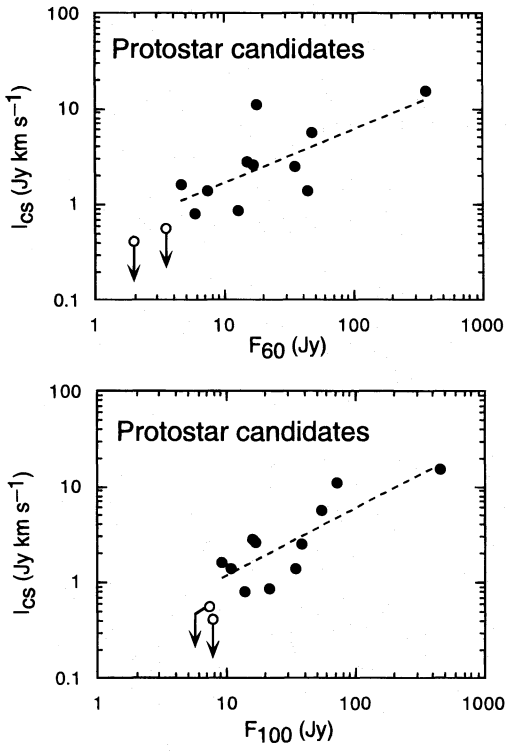

FIG. 13.—CS integrated intensity in Jy km s^{-1} toward all the 13 protostar candidates are compared with their *IRAS* flux densities at 60 μm (*top panel*) and at 100 μm (*bottom panel*). Open circles with an arrow have the same meaning as in Fig. 12. A dashed line in each panel shows the best fit to the 11 sources detected in CS by a least-squares fit.

among the T Tauri stars; the continuum emission is detected from two out of the 13 protostar candidates (15%), while it is detected from five out of the six T Tauri stars (83%). Such a difference was already reported in Paper I, although the number of samples was smaller in Paper I than in the present survey. Since the present result is consistent with the previous one with the number of samples being almost doubled, it is worth considering the significance of the difference in more detail. We first examine whether such a difference is real or merely due to some bias of the survey.

For the embedded protostar candidates, we observed all the 13 sources that were selected from the *IRAS* catalog with the well-defined criteria described in § 2. This means that the low-continuum detection rate toward the protostar candidates is significant. Even though our selection was biased toward relatively luminous embedded sources in the Taurus molecular cloud, this effect would strengthen the low continuum detectability among such sources, because we believe it natural that less luminous sources are statistically less massive and tend to have smaller disk masses than the luminous sources (e.g., Moriarty-Schieven et al. 1994).

On the other hand, the high continuum detectability toward the T Tauri stars may be due to a selection effect, because we selected T Tauri stars with strong fluxes both at 1.3 mm and 100 μm. Such a selection effect, coupled with our survey for T Tauri stars being far from complete, may explain why the observed T Tauri stars tend to have detectable 3 mm flux densities. However, we should raise the question of how meaningful it is to compare the result for the protostar candidates with that for the sample of all the T Tauri stars in the Taurus cloud. The evolutionary timescale of T Tauri stars is more than an order of magnitude longer than that for the embedded sources, so that we may expect that their disk masses, and thus the continuum detectability, vary significantly with their evolution. Recent observations of weak-line T Tauri stars actually showed that they tend to have disk masses smaller than classical T Tauri stars (Osterloh & Beckwith 1995). Because our main interest is in the disk mass in the earlier phase of protostellar evolution, it may be more appropriate that we discuss the present results among the sample of only young T Tauri stars and embedded sources. The observed five T Tauri stars except for DL Tau were, in fact, all younger than $10^{5.5}$ yr (e.g., Beckwith et al. 1990; Stapelfeldt et al. 1995).

For example, we may choose 18 T Tauri stars with ages less than $10^{5.5}$ yr cataloged by Beckwith et al. (1990) as a sample of "young" T Tauri stars. Evaluating the fraction of these young T Tauri stars with the 1.3 mm flux density larger than 157 mJy, which corresponds to the NMA detection limit of 12 mJy at 3 mm (3 σ) under the assumption of the power-law index of 3 for their flux densities, we found six T Tauri stars out of the 18. This gives an expectation value for the continuum detection rate of $\frac{1}{3}$. We may select another example of young T Tauri stars as those with disk luminosities greater than their stellar luminosities. Such T Tauri stars still have high mass accretion rates indicative of their youth. Among the 14 T Tauri stars selected by Lin et al. (1994) from the sample of Beckwith et al. (1990) under this criterion, six have a 1.3 mm continuum emission larger than 157 mJy, corresponding to the detection limit at 3 mm with NMA. This sample gives an expectation value of the continuum detection rate among young T Tauri stars greater than $\frac{1}{3}$. When the expectation value of $\frac{1}{3}$ was the same for emedded sources, we would expect at least four embedded sources to have detectable continuum emission at 3 mm, while we actually detected only two sources with NMA. This argument may be too crude, and we need to observe more T Tauri stars as well as to increase sensitivity in order to confirm the significance of the present results. Nevertheless, it leads us to suggest that the difference in the continuum detectability between the two types of objects is significant.

Recent sensitive observations of the 1.1 mm continuum emission from embedded protostar candidates confirmed our results that most of them have much smaller continuum emission (Moriarty-Schieven et al. 1994). They observed 12 of our sample protostar candidates and showed that eight sources have a 1.1 mm continuum flux density less than 200 mJy, corresponding to 9.3 mJy at 3 mm when we assume a spectral index of 3. The continuum flux from compact disks might be smaller than this value, if emission from extended envelopes within their beam size ($\sim$18.″5) contaminated the observed fluxes. This result implies that the difference in the continuum flux density between embedded sources and young T Tauri stars is much more significant than we have considered here.

5.4. *Implication of the Difference in the Continuum Detectability*

In Paper I we had a result consistent with the present study but with less significance, and argued the implication of the difference in the continuum detection rate between the observed embedded sources and T Tauri stars by

assuming the difference to be real. In this paper, because the difference in the continuum detectability between the two types of objects becomes more significant, we will consider its meaning in detail.

The flux density F_λ of optically thin dust continuum emission is a function of the total amount of matter (gas + dust) $M_{\rm gas+dust}$, the mass opacity of the dust grains κ_λ, and the dust temperature $T_{\rm dust}$[1],

$$F_\lambda = M_{\rm gas+dust}\,\kappa_\lambda\,B_\lambda(T_{\rm dust})\,\frac{1}{d^2}\,, \qquad (1)$$

where B_λ is the Planck function, and d is the distance to the object (Hildebrand 1983). Thus, there are three possible interpretations that explain the difference in the detectability of the continuum emission, viz., the difference in the total mass, that in the mass opacity of dust grains, and that in the dust temperature. The dust temperature around the embedded protostar candidates might be lower than that around the T Tauri stars, because the average bolometric luminosity of the T Tauri stars is ~ 3 times larger than that of the protostar candidates. This difference in bolometric luminosity is, however, not effective enough to cause a systematic change in the dust temperature around the two types of objects, because the factor of 3 change in luminosity corresponds to a difference in the radiative equilibrium dust temperature of only a factor of 1.3. The average flux density of the T Tauri stars detected at 3 mm is ~ 4 times larger than that of the protostar candidates not detected at 3 mm, meaning that a factor of 4 difference would be required for the dust temperature between the two types of objects; the observed T Tauri stars would be at least 2 orders of magnitude more luminous than the protostar candidates if the difference in the continuum detectability mainly depended on the difference in the dust temperature. It is therefore unlikely that the dust temperature is the main cause of the difference in the continuum detectability, so that the difference in flux density is either due to the difference in the total mass, or in the mass opacity, or in both.

5.4.1. *Systematic Difference in Disk Mass*

In Paper I we assumed that the difference in continuum detectability was due to the difference in the disk masses between the embedded protostar candidates and young T Tauri stars. Because embedded sources are considered to be an earlier evolutionary phase than T Tauri stars, this difference was naturally explained in terms of the increase of disk mass in the course of stellar evolution. We then pointed out that very young T Tauri stars in the Taurus molecular cloud should still keep accreting significant amounts of matter onto disks from their envelopes, which causes the rapid increase of disk mass through the evolution from invisible to visible objects. There are, in fact, several T Tauri stars showing flat spectral energy distributions which can be explained by the presence of infalling envelopes around them (Calvet et al. 1994). Moreover, recent ^{13}CO ($J = 1$–0) observations of HL Tau, one of the youngest T Tauri stars, have actually revealed a dynamically accreting gaseous disk around the inner disk observed in the dust emission (Hayashi et al. 1993). The mass accretion rate onto the central star/inner disk system was estimated to be 5×10^{-6} $M_\odot$ yr^{-1}, which was in good agreement with theoretically predicted values for embedded sources (Shu, Adams, & Lizano 1987; Kenyon et al. 1993). This suggests that young T Tauri stars, especially flat spectrum sources, still have large mass accretion rates from their (flattened) envelopes to the inner disks, supporting our disk-growing scenario derived from the present results. Theoretical calculations of disk growth also show that disk mass increases rapidly at the end of the main accretion phase in proportion to the square of the elapsed time from the onset of dynamical collapse (Nakamoto & Nagagawa 1995; see also Stahler et al. 1994).

We must note that the above arguments are valid only for the sources associated with the Taurus molecular cloud, where the scatter in mass of newly born stars is relatively small compared to, for example, those in the Ophiuchus cloud, and therefore the evolutionary effect is more significant than the difference in final stellar mass of young stellar objects. The difference in continuum flux between embedded sources and T Tauri stars would not be discussed as an evolutionary effect in molecular clouds or samples where we cannot distinguish the effect of stellar mass variation and evolution.

5.4.2. *Difference in Mass Opacity*

The other factor to cause the change in continuum fluxes between the protostar candidates and T Tauri stars is the mass opacity, which was not discussed in Paper I. If there is a systematic change in the mass opacity of dust particles between the two types of objects, we would expect a systematic difference in the observed flux density between them, even if their disk masses are on average the same. We derived the mass opacity at a millimeter wavelength λ by extrapolating its value at 400 μm, κ_{400}, which was determined by Keene et al. (1982), and assuming its power-law dependence on wavelength with the index β as $\kappa_\lambda = \kappa_{400}(400\ \mu{\rm m}/\lambda)^\beta$ (see § 4). We will summarize observational and theoretical works on the possible variation of both κ_{400} and β, and discuss whether such variation can account for our results.

In a diffuse interstellar medium, the value of β is usually assumed to be 2 at millimeter and submillimeter wavelengths because this dependence is consistent with the sum of rule derived by Purcell (1969). There has been a good amount of evidence that the β value for compact disks around T Tauri stars is smaller than this traditional one (Beckwith et al. 1986; Sargent & Beckwith 1987; Adams et al. 1990; Weintraub, Sandell, & Duncan 1989; Beckwith et al. 1990; Beckwith & Sargent 1991; Mannings & Emerson 1994). In particular, Beckwith & Sargent (1991) observed spectral shape at submillimeter wavelengths toward 29 T Tauri stars, deriving values of β from -1 to 1, which were significantly smaller than the ordinarily assumed value for diffuse interstellar clouds. Because the physical conditions in compact circumstellar disks around T Tauri stars is considerably different from those in diffuse clouds, it may not be surprising that such small β values are observed as a result of change of dust properties.

The β values for the compact disks around embedded sources are not easily measured, and the number of observations is still limited. Barsony & Kenyon (1992) observed

[1] We assume the constant gas-to-dust mass ratio of 100 in this discussion, although recent studies showed that the gas-to-dust ratio might change because of gas depletion (Skrutskie et al. 1993; Dutrey, Guilloteau, & Simon 1994; Aikawa et al. 1995).

10 protostar candidates in Taurus at 800 and 1100 μm with the 15 m James Clerk Maxwell Telescope (JCMT), finding that submillimeter SEDs of the protostar candidates were not much different from those of T Tauri stars. On the other hand, Moriarty-Schieven et al. (1994) suggested also from their JCMT observations at the same wavelengths that submillimeter SEDs for protostar candidates were steeper, corresponding to larger β values, than those of T Tauri stars. They derived the power-law index of the flux density for 16 embedded sources to be 2.5–4, which correspond to values of β of 0.5–2 if we assume that the emission is optically thin. Although this range of the β values seems to be smaller than the ordinary value of 2 as for the cases of T Tauri stars, Moriarty-Schieven et al. (1994) argued that the difference in the SEDs between the embedded sources and T Tauri stars was significant based on their error estimates with statistical tests. If the β value differs in the disks between embedded sources and T Tauri stars as in the manner described by Moriarty-Schieven et al. (1994), it might be possible that the compact disks around T Tauri stars are brighter at millimeter wavelengths than those around embedded sources, even though their disks have the same mass.

We must be careful, however, that single-dish observations might not reflect the true β value of compact disks for embedded sources because of the contamination from extended envelopes. Compact disks have a typical size of 1″ at the distance of Taurus, so that a large telescope beam, e.g., 18″.5 for JCMT at 1100 μm, dilute the emission from the disks while picking up all the fluxes from the envelopes. Thus, even if the envelopes are 2 orders of magnitude fainter in brightness than the disks, the contribution from the envelopes is not negligible. This argument becomes more easily understood when we consider the following example. Suppose that there is a protostellar envelope with a mass and radius of 4 $M_\odot$ and 0.1 pc, respectively, and that it has a density distribution proportional to $r^{-1.5}$, then the column density toward the center of this envelope averaged over the beam size of 18″.5 is 8.7×10^{22} cm^{-2}. If there is a compact disk whose mass is 0.1 $M_\odot$ at the center of this envelope, its beam-averaged column density is 5.0×10^{22} cm^{-2}. Thus, the contribution from the envelope to the total flux, which is proportional to the beam-averaged column density unless there is large temperature difference, would be comparable to that from the disk, and the submillimeter spectral index would reflect not only the spectral index of the disk, but also that of the envelope.

Interferometric observations are, on the other hand, less sensitive to extended structures because of their insufficient coverage of short baselines, and actually interferometric maps always show compact dust continuum emission even for the embedded sources that were observed to be extended in dust emission with single-dish telescopes (e.g., Ladd et al. 1991b; André & Montemerle 1994). Recently, Lay et al. (1994) observed the continuum emission at 870 μm toward L1551-IRS 5 and HL Tau with the JCMT-CSO interferometer, comparing the flux density at 870 μm with that of interferometric measurements at 2.7 mm. They found that both objects show the power-law spectral index of flux density to be $\sim$2.5, which indicates that the β value is less than 1 for the compact disks around L1551-IRS 5 and HL Tau. Chen, Zhao, & Ohashi (1995) derived a spectral index of $\sim$2.1 toward L1641-N, one of the embedded sources in Orion, from interferometric measurements at millimeter and centimeter wavelengths, suggesting a β value of 0.1 if the continuum emission is optically thin. These results favor similarly small values of β for the disks of both embedded sources and T Tauri stars, although the β value tends to be smaller than that for diffuse interstellar clouds. It is, for the summary of discussion about the β index, not adequate for us to conclude that the disk β index is different for the protostar candidates and the T Tauri stars.

The other possibility of changing the mass opacity between the two types of objects is its absolute value. We then discuss the difference in the absolute value of the mass opacity, i.e., κ_{400}, or more directly the opacity at millimeter wavelengths. The flux density for the T Tauri stars detected in this survey is on average 4 times larger than that for the protostar candidates without detectable continuum, which means that the mass opacities of dust particles differ at least by the factor of 4 between the two types of objects, if there is no systematic change in the disk mass between them. Theoretical estimates of the mass opacity showed that its probable range is over more than a factor of 30 (Draine 1989), so that it might happen that dust particles in the disks around young T Tauri stars systematically have larger mass opacity than those around embedded sources. It is, however, not easy to investigate what physical mechanism causes such a difference in the mass opacity, because the mass opacity of dust particles depends in a complicated way on their size, shape, and composition (Beckwith & Sargent 1991).

Miyake & Nakagawa (1993), calculating the mass opacity at millimeter wavelengths, considered a case where dust grains have a size distribution with a cutoff at various sizes between 0.01 μm and 100 m. They found that the mass opacity at millimeter and submillimeter wavelengths is enhanced when the cutoff size is between 1 mm and 1 cm. The estimated mass opacity at $\lambda = 1$ mm increases by a factor of $\sim$5 when the dust particles have the size distribution function $n(a) = a^{-3.5}$ (a is the radius of grains) with the cutoff at 1 mm.[2] Pollack et al. (1994), on the other hand, estimated the mass opacity of dust particles with various compositions and sizes between 0.1 μm and 30 mm. Their result showed that the mass opacity at $\lambda = 1$ mm tends to be enhanced at most by a factor of $\sim$4 when the dust size is between 300 μm and 3 mm, which is consistent with the result of Miyake & Nakagawa (1993).

The above two theoretical calculations suggest that the mass opacity at millimeter wavelengths becomes larger by a factor of 4–5 when the dust size becomes large ($\sim$1 cm) or the dust composition changes. It would therefore be possible to explain the difference in the 3 mm continuum detectability between the protostar candidates and T Tauri stars in terms of the difference in the mass opacity of dust particles between the two types of objects. This alternative interpretation of our result implies that the dust particles in disks, whose mass do not necessarily increase, may grow when the protostar candidates evolve into the T Tauri stars.

6. CONCLUSIONS

An interferometric survey of 13 protostar candidates and six T Tauri stars located in the Taurus molecular cloud has been made in 3 mm continuum and CS ($J = 2$–1) emissions using the NMA with a spatial resolution of 2″.8–10″. The main results are summarized as follows

[2] The refractive index with larger real part may produce a larger increase of the mass opacity (Miyake & Nakagawa 1993).

1. Two protostar candidates and five T Tauri stars had 3 mm continuum emission detected. The emission was not unresolved with the emission peaks well coincident with central sources, suggesting that the 3 mm continuum emission arises from circumstellar disks. The masses of the circumstellar disks were estimated to be 0.068–0.16 $M_\odot$ under the assumption of a gas-to-dust mass ratio of 100. We did not find a trend that sources with well-developed outflows have strong dust continuum emission.

2. Eleven protostar candidates and two T Tauri stars exhibited extended CS emission with a typical size of $\sim$2000 AU. Out of the 11 protostar candidates, seven sources have CS emission coincident with infrared or radio sources, indicating that CS gas traces the inner part of their protostellar envelopes. The CS emission around the other four protostar candidates was located away from known infrared sources. The CS emission from two T Tauri stars was weaker and less extended than that around the protostar candidates. The emission peaks were not coincident with the T Tauri stars, indicating that the CS emission may be the remnant dense cores from which they were formed. The higher detection rate of CS toward the protostar candidates than that toward the T Tauri stars is naturally interpreted as the dissipation process of dense cores in the course of protostellar evolution. The integrated intensities of CS for the protostar candidates is correlated with their bolometric luminosities, suggesting that stars with larger stellar mass are formed from more massive dense cores.

3. The CS emission around L1489 and IRAS 04365+2535 show disklike features with a velocity gradient along their major axes. The elongated disklike structure toward L1489 is $\sim$3000 AU in size and is nearly perpendicular to the outflow direction defined by single-dish observations with a large beam size, while IRAS 04365+2535 exhibits twin peaks separated $\sim$1000 AU away from each other with symmetric CS distribution with respect to the central star and the ridge of the compact outflow. The velocity gradient along the disklike structure of L1489 may be due to rotation of the disk, while the origin of that around IRAS 04365+2535 is not clear.

4. L1551-IRS 5 has compact CS emission, concentrated toward the central radio source, and weak extended emission, which may be a dense part of the molecular outflow. The compact CS emission shows a velocity gradient from north to south across the central star. The velocity gradient may be due to the outflow or possible infall rather than due to rotation of the disk.

5. The CS emission detected around L1527 is anticorrelated with the compact molecular outflow. This suggests that the CS emission may originate from a dense shell swept up by the outflow, even though the compact outflow does not have enough momentum to accelerate the CS dense shell.

6. The continuum detectability toward the protostar candidates is significantly lower than that statistically expected from the detection rate of dust disks around T Tauri stars. This low detectability suggests that, compared to T Tauri disks, circumstellar disks around the protostar candidates have smaller disk masses, or dust particles with larger mass opacity, or both. Such differences in the properties of circumstellar disks between the two types of objects may be naturally understood as an evolutionary effect; namely, in the course of the evolution from embedded protostars to revealed T Tauri stars, the disk mass has rapidly increased and/or the mass opacity has increased as a result of dust growth.

We are grateful to the staff members of NRO for their help during the observations and data reduction. We also thank Motohide Tamura for providing us with his outflow data on L1527 before its publication, and Naoto Kobayashi and Jim Emerson for their suggestion on infrared images of L1489. N. O. is supported by a Smithsonian Postdoctoral Fellowship.

APPENDIX A

DIFFERENCE IN THE DISK MASS ESTIMATED FROM DUST CONTINUUM EMISSION BETWEEN BECKWITH ET AL. (1990) AND THIS PAPER

Beckwith et al. (1990, hereafter BSCG) estimated disk mass from the flux density at 1.3 mm, while we estimated it from that at 3 mm. There are two differences in these mass derivation procedures that together result in a difference of derived mass up to a factor of $\sim$3.

1. Assumed values of the mass opacity at submillimeter wavelengths are different. Although BSCG and we both assumed $\beta = 1$ when extrapolating the mass opacities at submillimeter wavelengths to 1.3 or 3 mm, the referred submillimeter mass opacities were different. BSCG used the mass opacity of 0.1 cm^2 g^{-1} at 250 μm (Hildebrand 1983), while we adopted the mass opacity of 0.037 cm^{-2} g^{-1} at 400 μm (Keene et al. 1982). This is because Hildebrand's mass opacity at 250 μm was derived from Keene's 400 μm opacity under the assumption of $\beta = 2$. We used Keene's 400 μm value in order to be consistent with the $\beta = 1$ assumption used in deriving millimeter-wave opacities. This makes our mass opacity $\sim$1.7 times larger than BSCG's.

2. We assumed an entirely optically thin disk with a single temperature to calculate the mass, while BSCG estimated the disk mass through model fitting to spectral energy distributions with more plausible temperature and density distributions. When the disk mass of T Tauri is estimated from the 1.3 mm flux density (280 mJy) and opacity (0.02 cm^2 g^{-1}) of BSCG using our method with the dust temperature of 36 K, the derived mass is $\sim$1.6 times larger than that estimated by BSCG.

In addition to the above two different points in the mass derivation processes, BSCG's and our masses are different when an actual spectral energy distribution differs from that with $\beta = 1$. In the case of T Tauri, the actual spectral energy distribution prefers $\beta \sim 0$, while BSCG and we both assumed $\beta = 1$. This makes our mass 2.3 times larger than BSCG's. This effect together with the above differences in the mass derivation methods makes our mass estimate of the T Tauri disk $\sim$6 times larger than that of BSCG.

APPENDIX B

SPECTRAL ENERGY DISTRIBUTION OF T TAURI

Figure 14*a* shows the spectral energy distribution of T Tauri from centimeter to submillimeter wavelengths. The data for the plot is summarized in Table 8. Errors of the plots are at most the size of the plot markers. The SED is not fitted by a single

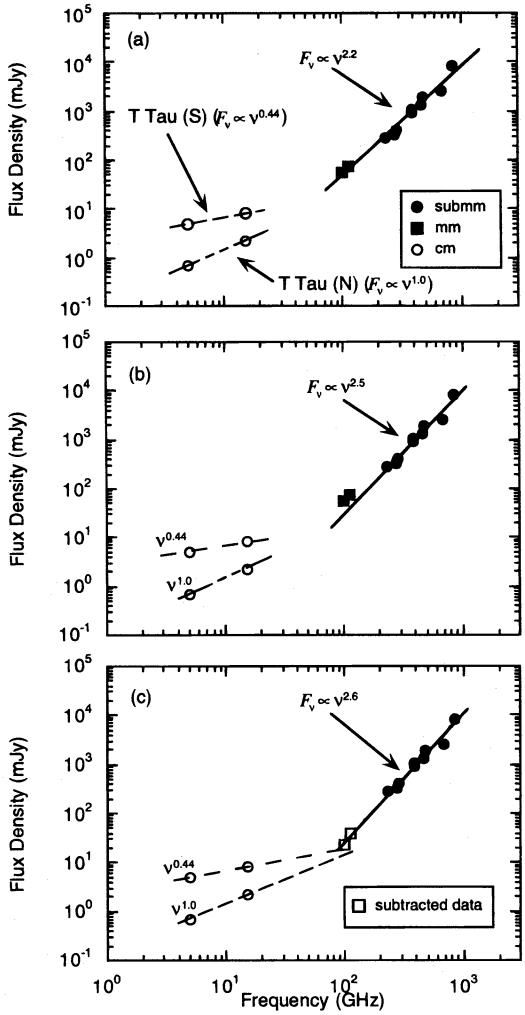

FIG. 14.—Continuum flux densities of T Tauri from submillimeter to centimeter wavelengths listed in Table 8 are plotted as a function of frequency. Filled circles, filled squares, and open circles indicate observed data at submillimeter, millimeter, and centimeter wavelengths, respectively. For centimeter wavelengths, data of T Tau (S) and T Tau (N) are individually plotted with their spectra of *free-free emission* estimated from the flux density at centimeter wavelengths by Schwartz et al. (1986). (*a*) The best fit to the observed data at millimeter and submillimeter wavelengths is indicated by the thick line. The derived spectral index is 2.2. (*b*) The best fit to the observed data at only submillimeter wavelengths is indicated by the thick line. The derived spectral index is 2.5. (*c*) The thick line shows the best fit to the observed data at submillimeter wavelengths and the *subtracted* data at millimeter wavelengths (*open squares*) estimated from both free-free emission spectra of T Tau (S) and (N) on the assumption that they continue up to 3 mm with the same spectra indices.

component; dust emission dominates at submillimeter wavelengths and free-free emission at centimeter wavelengths. The flux densities at frequencies larger than 100 GHz are well fitted by a power law $F_\nu \propto \nu^\alpha$ with an index of $\alpha = 2.2$, suggesting that the continuum emission at 3 mm may be due to dust emission. It might be possible, however, that the free-free emission contributes significantly to the 3 mm flux density, because the free-free emission at centimeter wavelengths is strong with positive spectral indices (Schwartz et al. 1986).

In order to estimate the contribution of the free-free emission to the 3 mm flux density, we fitted the SED of T Tauri using only submillimeter data. Figure 14*b* shows that the SED at submillimeter wavelengths is well fitted by a power law with an index of 2.5. Then the observed flux densities at 2.7 and 3 mm lie slightly above the extrapolated value from the submillimeter region with a power-law index of 2.5. Assuming that the free-free emissions from T Tau (N) and T Tau (S) could be extrapolated up to 3 mm with the same spectral indices as those in the centimeter region, we would expect that 32 mJy out of the total flux density at 3 mm is a free-free contribution. By subtracting this, we obtain the dust contribution of 24 mJy at 3 mm as shown by open squares in Figure 14*c*, which shows that the 3 mm flux is well approximated by the value extrapolated

TABLE 8

THE FLUX DENSITIES AT SUBMILLIMETER, MILLIMETER, AND CENTIMETER WAVELENGTHS FROM T TAURI

λ (mm)	ν_{eff} (GHz)	FLUX DENSITY (mJy)[a]			REFERENCE
		T Tau (N)	T Tau (S)	T Tau (Total)	
0.35.....	854			8500 ± 1000	1
0.45.....	676			2600 ± 400	1
0.6.....	481[b]			1840 ± 250	2
	463			1300 ± 200	1
0.8.....	390[b]			910 ± 90	2
	380			1070 ± 110	1
1.1.....	284[b]			417 ± 41	2
	272			320 ± 30	1
1.3.....	230			230 ± 9	3
2.7.....	112			75 ± 7.5	4
3.....	98			56 ± 10	5
20.....	15	2.2 ± 1.0	8.1 ± 1.0	10.3 ± 1.0	6
60.....	4.9	0.7 ± 0.5	5.0 ± 0.5	5.7 ± 0.5	6

[a] When errors were not shown in the literature, we referred to 1 σ values as error.

[b] This value was calculated from λ_{eff} in the literature.

REFERENCES.—(1) Adams et al. 1990; (2) Beckwith & Sargent 1991; (3) Beckwith et al. 1990; (3) Weintraub, Masson, & Zuckerman 1989; (4) this work; (5) Schwartz et al. 1986.

from submillimeter flux densities with the index of 2.5. This suggests the possibility that at most 60% of the total flux density at 3 mm is contaminated by the free-free emission, which reduces the disk mass of T Tauri derived in this paper by at most a factor of ~ 2.

REFERENCES

Adams, F. C., Emerson, J. P., & Fuller, G. A. 1990, ApJ, 357, 606
Adams, F. C., Lada, C. J., & Shu, F. H. 1987, ApJ, 312, 788
Aikawa, Y., Miyama, S. M., Nakano, T., & Umebayashi, T. 1995, ApJ, submitted
André, P., & Montmerle, T. 1994, ApJ, 420, 837
Barsony, M., & Kenyon, S. J. 1992, ApJ, 384, L53
Beichman, C. A. 1986, in Light on Dark Matter, ed. F. P. Israël (Dordrecht: Reidel), 279
Beichman, C. A., Myers, P. C., Emerson, J. P., Harris, S., Mathieu, R., Benson, P. J., & Jennings, R. E. 1986, ApJ, 307, 337
Beckwith, S. V. W., & Sargent, A. I. 1991, ApJ, 381, 250
Beckwith, S. V. W., Sargent, A. I., Chini, R. S., & Güsten, R. 1990, AJ, 99, 924
Beckwith, S., Sargent, A. I., Scoville, N. Z., Masson, C. R., Zuckerman, B., & Phillips, T. G. 1986, ApJ, 309, 755
Benson, P. J., & Myers, P. C. 1989, ApJS, 71, 89
Cabrit, S., & André, P. 1991, ApJ, 379, L25
Calvet, N., Hartmann, L., Kenyon, S. J., & Whitney, B. A. 1994, ApJ, 434, 330
Chen, H., Zhao, J.-H., & Ohashi, N. 1995, ApJ, 450, L71
Chikada, Y., et al. 1987, Proc. IEEE, 75, 9, 1203
Cohen, M., Emerson, J. P., & Beichman, C. A. 1989, ApJ, 339, 455
Cohen, M., & Kuhi, L. V. 1979, ApJS, 41, 743
Draine, B. T. 1989, in Proc. 22d and ESLAB Symposium on Infrared Spectroscopy in Astronomy, ed. B. H. Kaldeich (Noordwijk: ESA), 93
Dutrey, A., Guilloteau, S., & Simon, M. 1994, A&A, 286, 149
Dyck, H. M., Simon, T., & Zuckerman, B. 1982, ApJ, 255, L103
Edwards, S., Ray, T., & Mundt, R. 1993, in Protostars and Planets III, ed. E. H. Levy & J. I. Lunine (Tucson: Univ. Arizona Press), 567
Elias, J. H. 1978, ApJ, 224, 857
Emerson, J. P. 1988, in Formation and Evolution of Low Mass Stars, ed. A. K. Dupree & M. T. V. Lago (Dordrecht: Kluwer), 21
Emerson, J. P., & Moore, T. J. T. 1995, in Polarimetry of the Interstellar Medium, ed. D. C. B. Whittet & W. Roberge (San Francisco: ASP), in press
Hayashi, C., Nakazawa, K., & Nakagawa, Y. 1985, in Protostars and Planets II, ed. D. C. Black & M. S. Matthews (Tucson: Univ. Arizona Press), 1100
Hayashi, M., Hasegawa, T., Ohashi, N., & Sunada, K. 1994, ApJ, 426, 234
Hayashi, M., Ohashi, N., & Miyama, S. M. 1993, ApJ, 418, L71
Heyer, M. H., Snell, R. L., Goldsmith, P. F., & Myers, P. C. 1987, ApJ, 321, 370
Hildebrand, R. H. 1983, QJRAS, 24, 267
Hirano, N. Ohashi, N., Hayashi, M., Hasegawa, T., & Tamura, M. 1995, ApJ, submitted
Joint *IRAS* Science Working Group 1988, *IRAS* Point Source Catalog, Version 2 (Washington, DC: GPO)
Jones, B. F., & Herbig, G. H. 1979, AJ, 84, 1872
Kaifu, N., et al. 1984, A&A, 134, 7
Kawabe, R., Inatani, J., Kasuga, T., Ishiguro, M., Yamamoto, M., Yamaji, K., & Watasawa, K. 1990, in Proc. 3d Asia-Pacific Microwave Conference (Tokyo: IEICE), 217
Kawabe, R., Saito, M., Kitamura, Y., & Ohashi, N. 1996, in preparation
Keene, J., Hildebrand, R. H., & Whitcomb, S. E. 1982, ApJ, 252, L11
Keene, J., & Masson, C. R. 1990, ApJ, 355, 635
Kenyon, S. J., Calvet, N., & Hartmann, L. 1993, ApJ, 414, 676
Kenyon, S. J., Hartmann, L. W., Strom, K. M., & Strom, S. E. 1990, AJ, 99, 869
Kitamura, Y., Kawabe, R., & Ishiguro, M. 1992, PASJ, 44, 407
Ladd, E. F., Adams, F. C., Casey, S., Davidson, J. A., Fuller, G. A., Harper, D. A., Myers, P. C., & Padman, R. 1991a, ApJ, 366, 203
———. 1991b, ApJ, 382, 555
Lay, O. P., Carlstrom, J. E., Hills, R. E., & Phillips, T. G. 1994, ApJ, 434, L75
Lin, D. N. C., Hayashi, M., Bell, K. R., & Ohashi, N. 1994, ApJ, 435, 821
Linke, R. A., & Goldsmith, P. F. 1980, ApJ, 235, 437
Macleod, J., & Avery, L. 1995, in preparation
Maihara, T., & Kataza, H. 1991, A&A, 249, 392
Mannings, V., & Emerson, J. P. 1994, MNRAS, 267, 361
Miyake, K., & Nakagawa, Y. 1993, Icarus, 106, 20
Mizuno, A., Onishi, T., Hayashi, M., Ohashi, N., Sunada, K., Hasegawa, T., & Fukui, Y. 1994, Nature, 368, 719
Momose, M., Ohashi, N., Kawabe, R., & Hayashi, M. 1995, in Proc. Disks and Outflows around Young Stars, ed. S. V. W. Beckwith, A. Natta, & J. Staude (Berlin: Springer), in press
Moriarty-Schieven, G. H., Wannier, P. G., Keene, J., & Tamura, M. 1994, ApJ, 436, 800
Mundy, L. G., Wootten, A., Wilking, B. A., Blake, G. A., & Sargent, A. I. 1992, ApJ, 385, 306
Myers, P. C., Fuller, G. A., Mathieu, R. D., Beichman, C. A., Benson, P. J., Schild, R. E., & Emerson, J. P. 1987, ApJ, 319, 340
Myers, P. C., Heyer, M., Snell, R. L., & Goldsmith, P. F. 1988, ApJ, 234, 907
Myers, P. C., Linke, R. A., & Benson, P. J. 1983, ApJ, 264, 517
Nakamoto, T., & Nakagawa, Y. 1995, ApJ, 445, 330
Nakano, T., Hasegawa, T., & Norman, C. 1995, ApJ, 450, 183

Ohashi, N. 1991, Ph.D. thesis, Nagoya Univ.
Ohashi, N., Hayashi, M., Ho, P. T. P., Momose, M., & Hirano, N. 1996, ApJ, 466, in press
Ohashi, N., Kawabe, R., Hayashi, M., & Ishiguro, M. 1991, AJ, 102, 2054 (Paper I)
Ohashi, N., Momose, M., & Hayashi, M. 1995, in preparation
Osterloh, M., & Beckwith, S. V. W. 1995, ApJ, 439, 288
Pollack, J. B., Hollenbach, D., Beckwith, S., Simonelli, D. P., Roush, T., & Fong, W. 1994, ApJ, 421, 615
Purcell, E. M. 1969, ApJ, 158, 433
Rodríguez, L. F., Cantó, J., Torrelles, J. M., & Ho, P. T. P. 1986, ApJ, 301, L25
Rydgren, A. E., Schmelz, J. T., Zak, D. S., & Vrba, F. J. 1984, Publ. US Naval Obs., 25, 1
Sargent, A. I., & Beckwith, S. 1987, ApJ, 323, 294
Sargent, A. I., Beckwith, S., Keene, J., & Masson, C. 1988, ApJ, 333, 936
Schwartz, P. R., Simon, T., & Campbell, R. 1986, ApJ, 303, 233
Shu, F. H., Adams, F. C., & Lizano, S. 1987, ARA&A, 25, 23
Skrutskie, M. F., Dutkevitch, D., Strom, S. E., Edwards, S., & Strom, K. M. 1990, AJ, 99, 1187
Skrutskie, M. F., et al. 1993, ApJ, 409, 422
Snell, R. L., Loren, R. B., & Plambeck, R. L. 1980, ApJ, 239, L17
Stahler, S. W., Korycansky, D. G., Brothers, M. J., & Touma, J. 1994, 431, 341
Stahler, S. W., Shu, F. H., & Tamm, R. E. 1980, ApJ, 241, 637
Stapelfeldt, K. R., et al. 1995, ApJ, 449, 888
Strom, K. M., Strom, S. E., Edward, S., Cabrit, S., & Skrutskie, M. F. 1989, AJ, 97, 1451
Tamura, M., Gatley, I., Waller, W., & Werner, M. W. 1991, ApJ, 374, L25
Tamura, M., Ohashi, N., Hirano, N., Itoh, Y., & Moriarty-Schieven, G. H. 1995, in preparation
Tamura, M., Ohashi, N., Moriarty-Schieven, G., Hayashi, M., & Hirano, N. 1994, in Astronomy with Millimeter Wave Interferometer, ed. M. Ishiguro & W. J. Welch (San Francisco: ASP), 268
Terebey, S., Beichman, C. A., Gautier, T. N., & Hester, J. J. 1990, ApJ, 362, L63
Terebey, S., Chandler, C. J., & André, P. 1993, ApJ, 414, 759
Weintraub, D. A., Masson, C. R., & Zuckerman, B. 1989, ApJ, 344, 915
Weintraub, D. A., Sandell, G., & Duncan, W. D. 1989, ApJ, 340, L69
Yang, J., Ohashi, N., & Fukui, Y. 1995, ApJ, 455, 175